

A study of Asphalt Binders by X-Ray Diffraction Using Pearson-VII, Pseudo-Voigt and Generalized Fermi Functions

by

©Haifa Alqahtani

A thesis submitted to the School of Graduate Studies in partial fulfillment of the
requirements for the degree of

M.Sc.

**Department of Physics and Physical Oceanography
Memorial University of Newfoundland**

Memorial University of Newfoundland

2016

ST. JOHN'S

NEWFOUNDLAND

Abstract

Twenty-three asphalt binder samples were obtained from Northern Ontario, Alberta from Canada, Montana USA, and Venezuela. Structural studies of asphalt in crude oil have been performed by X-ray diffraction (XRD). The XRD spectra were taken with a Rigaku Dmax 2200V/PC, and JadeTM software was used for initial analysis. XRD implementation with Cu-K- radiation operating at 40 KV and 40 mA, with a scan rate of $0.001^\circ \ 2 \ \theta$ per second. The XRD data were fitted with (Pearson VII, pseudo-Voigt) profiles, and then modeled in Mathematica using a generalized Fermi function (GFF).

The results are discussed in terms of their accuracy with different combinations of backgrounds such as (Linear, Level, Fixed, Parabolic, 3^{rd} order Polynomial, 4^{th} order Polynomial). In addition, the fits also include various parameters, for example, Threshold Sigma, Intensity Cutoff, Range to find background, Exponent, Skewness and Lorentzian.

Abbreviations

X-ray Diffraction	XRD
Pearson VII	P
Pseudo – Voigt	V
Generalized Fermi Function	GFF
Full Width Half Maximum	FWHM
Hot Mix Asphalt	HMA
Cold Mix Asphalt	CMA
Warm Mix Asphalt	WMA
Street Cold Asphalt	SCA
Warm mix asphalt concrete	WAMC
Asphalt Cement	AC
Performance Grade	PG
Petroleum Asphalt Heavy	PA-H
Polycyclic Aromatic Hydrocarbon.....	PAH
Small Angle Neutron Scattering.....	SANS
Small Angle X-ray Scattering.....	SAXS
X-ray Photoelectrons Spectroscopy.....	XPS
Strategic Highway Research Program	SHRP
American Association of State Highway and Transportation	AASHTO

Table of Contents

Abstract	ii
Abbreviations	iii
Table of Contents	vi
List of Tables	vii
List of Figures	x
1 Introduction	1
1.1 Asphalt and Asphaltene.	1
1.1.1 Properties of Asphaltene.	2
1.1.1.1 Physical Properties and Characteristics of Asphaltenes.	4
1.1.2 Types of Asphaltene.	5
1.1.2.1 Natural Asphalt.	7
1.1.2.2 Petroleum Asphalts.	8
1.1.2.3 Asphalt Cement.	9
1.1.3 Performance Grade (PG).	9
1.1.4 Rutting and Cracking.	10
1.1.4.1 Fatigue Cracking.	11

1.1.4.2	Rutting.	12
1.2	X-ray Diffraction (XRD) Measurements.	13
1.2.1	X-Ray Scattering Theory.	13
1.3	Asphaltene Structure and X-Ray Diffraction.	14
1.3.1	Modeling Asphalt as a Cubic Material (Yen-Model).	16
1.3.2	The Modified Yen Model.	17
1.4	SAXS and SANS.	19
2	Experimental	21
2.1	Setup Components.	21
2.2	Sample Preparation for XRD.	24
2.2.1	Method of Powder XRD.	24
2.2.2	Method of Thin Film XRD.	24
2.3	Spectral Line Shapes Modeled Using Mathematical Functions.	25
2.4	Pearson VII and Pseudo-Voigt.	27
2.5	Generalized Fermi Function Applied to the Experimental X-Ray Line Profile Analysis.	28
2.6	Exponential Asymmetric Blend Based upon Voigt-type Line-Shapes. . .	29
2.7	Line Shapes Analysis Using Peak Search and Profile Fit.	29
3	Results and Discussion.	30
3.1	X-ray Diffraction Patterns.	32
3.2	XRD Peak Search and Peak Profile Fitting.	37
3.3	Influence of Peak Shape Functions.	37
3.4	XRD types with Different Backgrounds and Effect of Backgrounds. . .	41
3.5	Spectral Line Shapes Analysis.	46
3.5.1	Samples figures with GFF.	46

3.6	Comparing of XRD Results for Asphalt.	52
4	Conclusions	54
5	Recommendations for Future Work	56
6	Appendices	57
6.1	Proceedings for Profile Fitting a Diffraction Patterns.	57
6.2	GFF routine using Mathematica.	58
	Bibliography	70

List of Tables

1.1	Elemental Composition of Asphaltene from World Sources [6].	3
2.1	Pertinent Asphalt Binder Properties [23]	26
3.1	Aromaticity and Crystallite Parameters for Asphalt Binder Samples Calculated Using Pearson-VII(P), Pseudo-Voigt(V), and Generalized Fermi (GF) Function.	31
3.2	The Effect of Background on fit	44
3.3	Aromaticity and crystallite size for three samples, four backgrounds using Pearson-VII(P), Pseudo-Voigt(V), and Generalized Fermi Function(GFF).	45

List of Figures

1.1	Schematic layers of pavements [1].	2
1.2	Trinidad lake asphalt [2].	8
1.3	Damage in the wheel track as a result of fatigue failure, in a further phase fatigue cracks [3].	11
1.4	Rutting under highest tonnage and high temperatures [3].	12
1.5	Damages in a highway asphalt pavements and the traffic effect [4]. . . .	12
1.6	Asphalt schematic model of the chemical structure and crystal parame- ters. [16].	15
1.7	(a) XRD pattern of asphaltene, (b) planes corresponding to the peaks in the XRD pattern [16].	17
1.8	The Modified Yen model with its predominant asphaltene molecular hierarchy [31].	18
1.9	Proposed asphaltene molecular structures [31].	19
2.1	Cross-Sectional View of Diffraction of X-Rays by an Asphaltene Cluster [25].	22
3.1	Paradigms T1 and T2 for the XRD profile	32
3.2	Paradigms T3 and T4 for the XRD profile	32
3.3	Paradigms T5 and T6 for the XRD profile	33

3.4	Paradigms T7 and L1 for the XRD profile	33
3.5	Paradigms L2 and L3 for the XRD profile	33
3.6	Paradigms L4 and L5 for the XRD profile	34
3.7	Paradigms L6 and L7 for the XRD profile	34
3.8	Paradigms O1 and O2 for the XRD profile	34
3.9	Paradigms H1 and H2 for the XRD profile	35
3.10	Paradigms AEE and E9 for the XRD profile	35
3.11	Paradigms N1 and N2 for the XRD profile	35
3.12	Paradigms N3 for the XRD profile	36
3.13	Gauss and Lorentz peak shape function [34].	40
3.14	Samples T1 for the best peak.	43
3.15	Samples T3 for the best peak.	43
3.16	Samples T5 for the best peak.	43
3.17	Samples L2 for the GFF profile	46
3.18	Samples L3 for the GFF profile	46
3.19	Samples L4 for the GFF profile	46
3.20	Samples L5 for the GFF profile	47
3.21	Samples L6 for the GFF profile	47
3.22	Samples L7 for the GFF profile	47
3.23	Samples T1 for the GFF profile	47
3.24	Samples T2 for the GFF profile	48
3.25	Samples T3 for the GFF profile	48
3.26	Samples T4 for the GFF profile	48
3.27	Samples T5 for the GFF profile	48
3.28	Samples T7 for the GFF profile	49
3.29	Samples O1 for the GFF profile	49

3.30	Samples O2 for the GFF profile	49
3.31	Samples N1 for the GFF profile	50
3.32	Samples N2 for the GFF profile	50
3.33	Samples N3 for the GFF profile	50
3.34	Samples H1 for the GFF profile	51
3.35	Samples H2 for the GFF profile	51
3.36	Samples E9 for the GFF profile	51
3.37	Relationship between crystalline L_a and L_c for full width at half maximum (FWHM) [38].	53

Chapter 1

Introduction

1.1 Asphalt and Asphaltene.

Asphalt binder is one of the crucial elements in the construction of asphalt pavements. More than 90% of the roads in the United States of America are paved with asphalt. Asphalt is a by-product of the distillation process of crude oil and consequently it consists of various hydrocarbons, and includes the most polar, most aromatic, and highest molecular weight components of crude oil. Furthermore, it has a complex chemical structure that results in its complex physical and rheological behavior.

Asphalts are very complex and not well-characterized materials, also containing saturated and unsaturated aliphatic and aromatic compounds of up to 150 carbon atoms. Their composition varies depending on the provenance of crude oil. A lot of the compounds include oxygen, nitrogen, sulfur, and other heteroatoms.

Asphalt usually comprise about 80% by weight of carbon, 10% hydrogen, 6% sulfur, a few amounts of oxygen and nitrogen, and trace amounts of metals like iron, nickel, and vanadium. Further, the molecular weights of the constituent compounds range from hundred to many thousands.

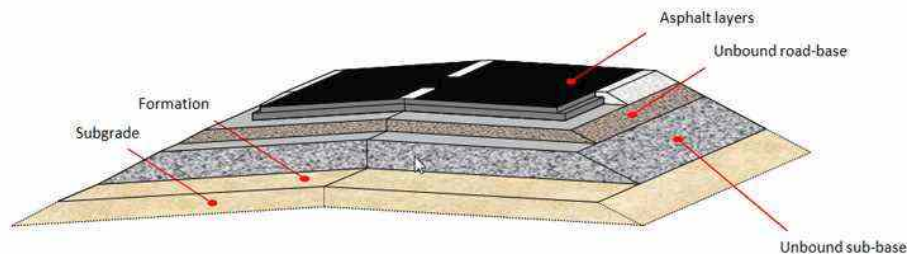


Figure 1.1: Schematic layers of pavements [1].

Asphaltenes are existing in most petroleum materials, and in all heavy oils and bitumen from oil sands. This material is expressed by solubility: the components that dissolve in toluene and precipitate in n-alkane solvents are the asphaltenes. Also, for the analytical purposes, the concentration of the asphaltene in crude oil is defined by precipitation with either n-pentane (C5) or n- heptane (C7).

Asphalt deposits can be extracted through petroleum production, and upgrading operation due to changes in temperature composition and pressure. A lot of scholars propose methods that can be applied to investigate, behavior at the experiment and analysis of the aging of organic compounds, and the vaguest part of bitumen component asphalt, using the X-ray diffractions. Yen and others achieved one of the most significant studies in asphaltene. [5].

1.1.1 Properties of Asphaltene.

Nations from all over the world are repeatedly trying to discover and extract crude oil from a new exporter. As a result, there is a massive variability in the physical and chemical properties of crude oil and even in the physical and chemical properties of crude oil and even greater variability in the remains after distillation such as asphalt binder.

Speight(1999) clarified asphaltene as the fraction separated from crude oil or petroleum

Source	Composition(Wt%)					Atomic Ratios				
/	C	H	N	O	S	H	/C	N/C	O/C	S/C
Canada	79.0	8.0	1.0	3.9	8.1	1	0.21	0.011	0.037	0.038
Iraq	80.6	7.7	0.8	0.3	9.7	1	0.15	0.0009	0.003	0.045
Kuwait	82.2	8.0	1.7	0.6	7.6	1	0.17	0.017	0.005	0.035
Mexico	81.4	8.0	0.6	1.7	8.3	1	0.18	0.006	0.016	0.038
Sicily	81.7	8.8	1.5	1.8	6.3	1	0.29	0.016	0.017	0.029
USA	84.5	7.4	0.8	1.7	5.6	1	0.05	0.0008	0.015	0.025
Venezuela	84.2	7.9	2.0	1.6	4.5	1	0.13	0.020	0.014	0.020

Table 1.1: Elemental Composition of Asphaltene from World Sources [6].

products upon addendum of hydrocarbon solvents such as n-heptane [6]. An elemental composition of asphaltene is shown in Table 1.1

The chemical composition of asphalt is very complex, comprising mainly carbon (80-88%) and hydrogen atoms (8-12%). Other elements, such as sulfur (0-9%), oxygen (0-2%), nitrogen (0-2%) have also been reported to be present, as well as trace amounts of vanadium, nickel, and manganese. Also, asphalt is composed of diverse organic and inorganic compounds. The structural complexity of bitumen itself has added to the overall complexity of asphalt.

Understanding the chemistry and microstructure of asphalt is critical in the development of performance-based specifications. The environmental factors cause asphalt corrosion and correlation moisture effects. The conditioning schemes used in the specifications requirement to reflect the environment more accurately. Subsequently, current oxidation models must be modified, and new samples must be sophisticated to reflect the impacts of moisture on asphalt pavements.

In this time, techniques are being developed to evaluate the phase behavior of con-

ventional classical and modified asphalts. Among these are microscopic techniques, such as, the atomic force microscope. This powerful surface analysis technique has a three-dimensional spatial ruling in the angstrom range.

1.1.1.1 Physical Properties and Characteristics of Asphaltenes.

Testing for quality monitoring and acceptance likely will keep on to concentrate on the bulk properties of asphalt binders, even though the existence of the metallic surface is widely accepted as converting the bulk properties. In the future developments in test methods and instrumentation will undoubtedly provide the paraphernalia for realization the role of the metal surface in the conduct and durability of asphalt binders. In situ characterization will be needed to fully comprehend the interaction between asphalt binders and the mineral surface as well as its significance to mixture and pavement performance.

Asphalt can be classified by its chemical installation and physical properties. The pavement industry typically depends on physical properties for rendering characterization although an asphaltene physical properties are a direct consequence of its chemical installation. The most important physical properties are durability, rheology, safety, and purity.

- **Durability.**

Durability is the measure of how asphalt physical properties change with age. In general, as an asphalt binder ages, its viscosity increases, and it becomes more stiff and brittle.

- **Rheology.**

Rheology is the studying of deformation and flow of matter. Deformation and flow of the asphalt binder in HMA is necessary for HMA pavement performance. Pavements that distort and flow too much may be liable to rutting and bleeding while those that

are too solid may be susceptible to tiredness cracking. HMA Pavement deformation is closely related to asphalt rheology. Rheological properties of asphalt vary with temperature, so rheological characterization includes two key considerations. Firstly, to fully characterize an asphalt binder, its rheological properties ought to be examined through the range of temperatures that it may be confronted during its life. Secondly, to compare various asphalt binders, their rheological properties must be the measurement at some common reference temperature.

- Safety.

Safety asphalt of cement like most other petroleum products can volatilize when heated. At extremely high temperatures (well over those experienced in the manufacture and construction of HMA) asphaltene cement can release enough steam to increase the volatile concentration straight above the asphalt binder cement to a point where it will ignite when exposed to a spark or open flame. This called the flash point. For safety reasons, the flashpoint of asphalt cement is examined and surveillance.

- Purity.

Asphalt cement, as used in paving, must consist of roughly pure bitumen. Impurities are not active cementing constituents and may be prejudicial to asphalt performance.

1.1.2 Types of Asphaltene.

Asphalt is most well known as a street road and highway coverage more technically called asphalt concrete, but there are a few various types in which the essence may appear. It is a naturally occurring material present in crude oil and naturalistic deposits, notably around particular bodies of water and in oil sands. This material is found in either liquid or semi-rigid form in nature and is characterized by its high viscosity and its sticky, black manifestation. It consists almost exclusively of bitumen, a material

composed of polycyclic aromatic hydrocarbons (PAHs). Asphalt has many types, some types of the asphalt are as follows:

- Hot Mix Asphalt (HMA).

To a large degree used for its convenience, hot mix asphalt, is the most common used elastic pavement. As well known as blacktop or bitumen, and sometimes hot mixture. Hot mix asphalt pavements are categorized mainly as dense-graded mixes, stone matrix mixes, and open-graded hot mix asphaltene. There are also other kinds of asphalt but are limited to conservation and rehabilitation works. Hot mix asphalt concrete (HMAC) produced at 320°F (160°C). This high temperature serves to diminish viscosity and dampness through the manufacturing process, resulting in a very strong material. Hot Mix Asphalt is most generally used for high-traffic areas, example busy highways and airports.

- Warm Mix Asphalt (WMA).

Warm mix asphalt is a different operation for admixture, hauling, placing and compaction asphalt mix using hot mix asphalt. WMA is the term used on technologies used to reduced temperatures prerequisite to producing and built-in asphalt mixtures on construction pavements. Generally, WMA uses temperatures ranging from (30° to 70°F) while mixing and could stay lower when applying. Once the asphalt has been placed it solidifies as it happens to HMA to form the pavement. Once it has been cooled perfectly, there will be no difference between hot mix asphalt and warm admix asphalt.

- Warm Mix Asphalt Concrete (WMAC).

These decrease the temperature desired for the industry by adding emulsions, waxes, or zeolites. This process benefits both the environment, as it results in less fossil fuel consumption and reduced release of fumes. In WMAC, the asphalt is emulsified in soapy water before blending it with the synoptic, eliminating the need for high

temperatures completely. However, the resulting material is not roughly as durable as HMAC or WAM, and it is commonly used in low traffic areas or to patch damaged HMAC.

- Cold mix asphalt (CMA).

Street Cold Asphalt is a high-quality, polymer-modified CMA obtainable in batch instructions to builders, road renovation municipalities, business owners . Cold asphalt changes everything. Street Cold Asphalt (SCA), is a comparatively new produce developed in 1995 during the introduction of new polymer technology into the manipulation in viscosity and substances designing, of the various components of an asphalt admix. SCA or CMA is soft and sticky out of the bag, but it fast hardens after application and the result is a pavement patch with better strength but analogous properties to HMA. There are some reasons for makes cold asphalt the best road patch solution. The first, cold patch, also known as a cold mix or cold asphalt (CMA or CA), was first known as a way to make way repairs speedily because it can be applied right from the container without heating. Second, it does not need any special heavy rolling machines or special applicators as it can be swept or poured into a pothole or utility split and tamped down with a hand tool.

1.1.2.1 Natural Asphalt.

Asphalt can be found in nature either as a pure form or in rock deposits. In the latter form, rocks such as sandstone are the major constituent of the material and asphalt represent only a small portion shown in figure (1.2). Examples of natural asphalts include Grahamite, Wurtzite, Trinidad [2] and Gilsonite. Of these natural examples of asphalts, Trinidad and Gilsonite haven been commercially used. Trinidad has been extensively used in road constructions. Trinidad is normally extracted from lakes in the island of Trinidad and contains, in its pure natural form, 40% asphalt and 60%

water and clay. Gilsonite is a naturally occurring asphalt having the characteristic of being very hard (zero penetration). This type of natural asphalt has been mainly used in asphalt paints and other commercial usages. One of the main characteristics of natural asphalt is that their sticking ability can be lost when being oxidized.



Figure 1.2: Trinidad lake asphalt [2].

1.1.2.2 Petroleum Asphalts.

Asphalt known as bitumen is a viscous black and highly viscid liquid or semi-solid form of petroleum. It may be found in naturalistic deposits or may be a refined product; it is a material classed as a pitch. The essential use 70% of asphalt/bitumen is in road build, where it is used as the glue or binder mixed with general particles to generate asphalt concrete. Its other fundamental uses are for bituminous waterproofing products, including the production of roofing felt and for stamping flat roofs. The terms asphalt and bitumen are predominantly used interchangeably to mean both natural and manufactured forms of the substance.

In America, asphalt cement is the carefully refined remains from the distillation operation of selected crude oils. The refining of petroleum is currently considered the major source of asphalt. The heavier component of crude oil is asphalted. Crude oil which comprises many different hydrocarbons can be classified, depending on their components, into two types: namely paraffin wax and mixed base crudes. In the

former type, a paraffin wax is produced upon the distillation of the volatile constituent of the crude oil. As the name suggests in the latter type, a combination of paraffin wax and asphalt constitute the heavier component of the crude oil. The refining of petroleum to obtain asphalt can be performed by a number of different approaches. The selection of the appropriate refining method depends on the type of the crude oil (i.e.: paraffin or mix). The most common methods used in the refinery process are distillation and solvent deasphalting. In the former method, heating the oil is first implemented following by the vacuum to complete the distillation process. The latter method, which is frequently used to generate paving asphalt, requires the use of a solvent to produce asphalt from the mix based crudes that have complex chemical structure.

1.1.2.3 Asphalt Cement.

Cement is the limestone-based powder that binds and hardens when mixed with water. In concrete, cement is the essential binding agent holding together the rest of the mixed. It is usually light gray. Also, asphalt cement (AC) are highly complicated mixtures a huge number of different chemical and species of hydrocarbon molecules whose thermic conduct is of essential importance for petroleum and road industry. Asphalt cement now called Performance Grade (PG) binders. Selected by climate and traffic at the location where it is intended to be used.

1.1.3 Performance Grade (PG).

The Performance Grade (PG) system is the method of categorizing an asphalt cement binder used in asphalt pavement relative to its rated performance at various temperatures. It was originally developed during the Strategic Highway Research Program (SHRP) in the early 1990's and was called "SuperPave TM." Performance grading is

based on the notion that asphalt binder properties must be related to the status under which the binder is used including air and pavement temperatures, and specific application for that particular facility.

The physical properties of asphalt cement change with temperature, i.e. asphalt cement is stiffer at lower temperatures and relatively softer at higher temperatures. PG asphalt binders are categorized and selected to meet performance criteria at expected high and low-temperature extremes with a confirmed level of reliability. PG impedes the permanent deformation or rutting at high temperatures and the resistance to transverse thermal cracking at low temperatures.

PG binder specifications require the asphalt to be modified with polymers or other chemicals to promote its properties and meet performance requirements. Adding these modifiers, however, have unfavorable consequences, i.e., by reducing the temperature susceptibility and age hardening. Also, the advantage of these kinds of a binder is that, they resist low temperature cracking and improve the hardness of the asphalt at high temperature, hence reducing rutting. The economic aspect of modified asphalt is far reaching since it can cost nearly twice as much as unmodified asphalt [7].

1.1.4 Rutting and Cracking.

Two of the fundamental phenomena that influence asphalt pavement performance are fatigue and rutting. Rutting is characterized by deformation of the pavement. It mostly evolves during the hot seasons, when the asphalt is softer, while fatigue cracking is characterized and occurs during mild cold seasons. It is believed that, for improving the fatigue and rutting performance of an asphalt binder pavement, comprehensive studies of the structural of asphalt binder at its microscopic level are to be decisive [7].



Figure 1.3: Damage in the wheel track as a result of fatigue failure, in a further phase fatigue cracks [3].

1.1.4.1 Fatigue Cracking.

Fatigue cracking failure is usually defined as a failure resulting from the repetitive action of loads and in pavements the loads outcome from traffic movement over the pavement. Commonly, failure to be visible, only after a long number of load recurrence, and results initially in the formation of small cracks. These small cracks are initially found in the wheel track and appear as a network of fine cracks. Various steps have been described in the fatigue failure operation: namely the initiation of minor hairline cracks, then by the evolution of these micro-cracks into wider macroscopic cracks, which coalesce and shape a network of cracks. In the last step, these microscopic cracks proliferate through the thickness of the pavement and leading to catastrophic failure resulting in the damage of structural safety of the road base. For example, of the final steps of fatigue cracking failure is shown in figure (1.3), where in this state, the cracked material has already induced the forming of a pothole. They sometimes are known as alligator cracks and can be recognized by the pattern of interconnected chaotic in the pavement surface. Galal and White, on (2001) reported that low temperature is responsible for fatigue and can be accelerated by pavement again. Hence, the major possible causes of fatigue cracking can be increased loading, inadequate structural design, and the most crucial of all is mix composition [8].



Figure 1.4: Rutting under highest tonnage and high temperatures [3].



Figure 1.5: Damages in a highway asphalt pavements and the traffic effect [4].

1.1.4.2 Rutting.

Rutting is one of the most significant distresses in the asphalt binder pavements, particularly in higher summer temperatures and/or under heavy cargo. The characteristic of the rutting on every asphalt binder pavement layer was analyzed by surveying the rutting depth, drilling transverse profile sections, and boring samples in the idealistic portions of expressways where various grades of rutting damage were observed. It noted that 60% of the rutting was generated by the asphalt middle course layer and the residual 40% came from the other surface layers, which was suitable for the mechanical analysis of the asphaltene binder pavement that showed that the shear stress in middle asphalt course layer was the highest in magnitude, under highest tonnage and high temperatures shown it in figures (1.4), (1.5).

Rutting is the load-induced lasting distortion of asphalt pavements and may occur in any layer of a pavement structure. It is one of the most significant distressed occurring in asphalt pavements and severely affects the comfortability, chauffeur safety, and general performance. With the augmentation in both traffic volume and weight overloading, the asphalt pavement rutting problem has become more and more dangerous. Under the function for example factors as heavy loading and poor weather that happened to several highway asphalt pavements, serious damages in terms of rutting appeared shortly after starting to traffic.

1.2 X-ray Diffraction (XRD) Measurements.

X-ray's and X-ray diffraction are important scientific phenomena and method when applied to experimental research. X-ray can be generated by electron shell transition in atoms. When X-ray photons collide with electrons, several of the photons from the incident ray be deflected. If the wavelength of these scattered X-ray didn't change i.e., X-ray photons didn't lose any energy. The operation is called elastic scattering (Thompson Scattering) where the only momentum has been transferred during the scattering operation. These are the X-rays that we measurement in diffraction experiments, as the scattered X-ray carry information about the electron apportionment in the film of the asphalt binder specimen.

1.2.1 X-Ray Scattering Theory.

Extremely collimated beam, combined with a long distance between the specimen and the detector, allow a sensitive measure of the X-ray that is just barely scattered by the model the scattering angle ($< 6^\circ$). Bragg's law is given as the following equation:

$$n\lambda = 2d \sin \theta \quad (1.1)$$

Where the length d is inversely proportionate to the scattering angle, thence small angle represented larger features in the samples. However, analysis the collected data of asphalt is determined by presumption of the Yen model. The atoms are rearranging themselves in a periodic method and a plain cubic structure for asphalt with four known peaks.

1.3 Asphaltene Structure and X-Ray Diffraction.

One of the primary and most critical studies in asphaltene is done by Yen and others [5,9–11,14]. They used X-ray analysis of asphalt to define the structure of asphalt. Yen with his co-workers scrutinized asphalt using X-ray diffraction, and they achieved that according to their measurements, asphalt is composed of a pile of clusters of n-alkanes. A senior margin of error of the X-ray diffraction sign collected to the aromatic clusters and causes an enormous of uncertainties that improve to the degree of concentricity [9].

In (1974), Yen suggested the first model and it is called the Yen Model, of the asphaltene’s structure that assumption simple cubic structure model as a grounds [10]. Nevertheless, this paradigm has been by many researchers, but Yen with his cooperators genuine idea has constantly been receiving attention for the last years. Moreover, they reported that robust chemical forces are responsible for asphaltenes element like hydrogen, carbon, and heteroatoms to retain them together [10].

XRD has been vastly used to study the microstructure of asphalt by Yen and others (1961) [11]. Sadeghi et al. reviewed the essential principles of the XRD for asphaltenes [14], along with Christopher with his colleagues (1996) and Shirokoff and others (1997), [12, 13]. Studies on asphaltenes macrostructure and crystallite param-

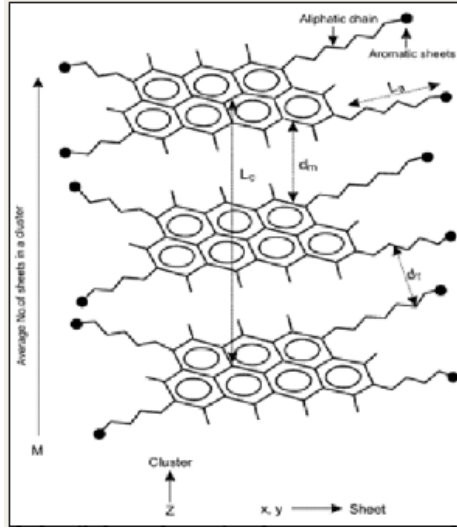


Figure 1.6: Asphalt schematic model of the chemical structure and crystal parameters. [16].

eters using XRD and NMR methods and presentation show that there is the interconnection between the information collected from XRD and NMR. XRD method is one of the essential techniques that provides knowledge about the microstructure and crystallite parameters of the asphalt. The description of X-ray consequence of carbon compounds fundamentally depends on the experimental results of both aromatic and waxes of hydrocarbons in different concentrations (Sadeghi et al., 1986) [11–14].

Michael et al., at (2005) gives a summary of the aromaticity and crystallite parameters, such as the average distance between the aromatic sheets d_M , the average distance between the aliphatic chains d_γ , the average diameter of the aromatic sheets L_a , the average diameter of the cluster L_c , the average number of aromatic sheets per cluster M_e , as figure (1.6) [15,16]. In (2002) Siddiqui and others, investigated crystallite parameters of asphalt by categorizing the samples as fresh and aged Arabian asphalt [16]. The structural transformations of asphalt molecules in thermal processing of vacuum residue by XRD extensively studied by Michael and others at (2005). Additional to that, these researchers, determine the microstructure and aromaticity

parameters using XRD and compared them with the average structural parameters calculated from NMR [15, 16].

Sadeghi et al. (1986) summarized the essential theory and implementation of XRD for asphalt description [14]. Moreover, based on an XRD study, Yen and Dickie (1967) suggested a microstructure which represent crystallites and particles of asphalt [9]. Schwager and others, (1983) examined the microstructure and crystallite parameter of various asphalt specimens and used NMR and XRD procedure to assessment the size of the average aromatic structural unit and the number of such units for each molecule [9, 14, 17].

XRD studies on asphaltenes by Decroocq et al. (1992) showed structural conversions through heat treatment, which is based on the change in peak position and density of the (γ) and (002) bands. Ebert et al. (1983) reported XRD of wax and stacked aromatic molecules and described the problems of determining the average structure of asphalt [19]. Based on the XRD pattern of various paraffins, naphthenes and aromatics, the author and coworkers showed that the (γ) band originates from paraffinic ordering and that the carbon atoms that aren't in stacks do not contribute to (002) band [18, 19].

1.3.1 Modeling Asphalt as a Cubic Material (Yen-Model).

There are four peaks in the XRD patterns of asphaltene. The peak (200) or graphene peak comes from the diffraction of X-ray by the stacks of aromatic molecules (Siddiqui and others, (2002) [16]. The peak (11) and peak (10) in the diffraction of X-ray are X-ray from the plane structure of the aromatics it is shown in figure (1.7). The peak (γ) is thought to be the packing distance of saturates which arises from x-ray scattered by aliphatic chains or condensed saturated rings [16].

The wider the peaks in the XRD patterns, the more short range order and less

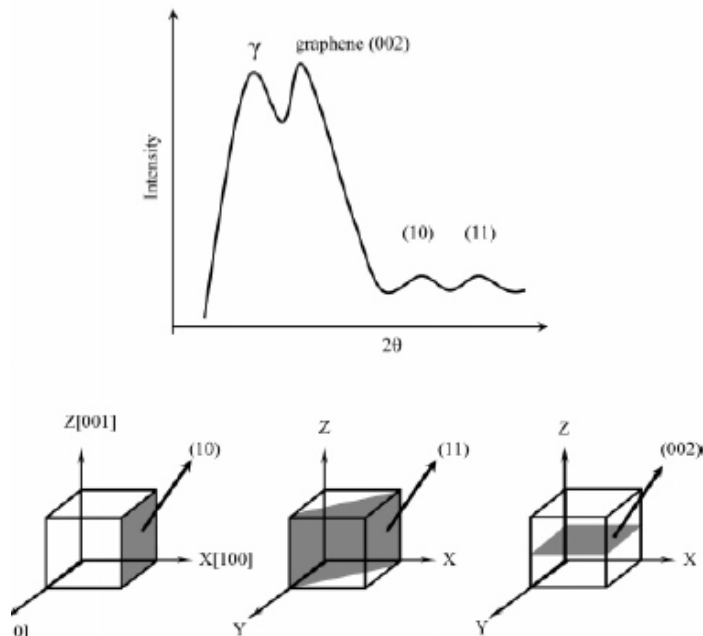


Figure 1.7: (a) XRD pattern of asphaltene, (b) planes corresponding to the peaks in the XRD pattern [16].

long range order that exists in the structure. Generally, sharp narrow XRD pattern peaks are from highly crystalline specimens with a high degree of long range order. In the case of asphalt, there is a good long range order in some directions in the solid crystals, and only short range order in others. This is the obvious reason for why there are sharp and broad peaks in all the diffraction patterns.

1.3.2 The Modified Yen Model.

The modified Yen model consists of a first-principles approach in treatment the hierarchical structures of and characteristics manifested by asphaltenes. As such, the asphaltenes molecular structures are absolutely key. The modified Yen model is shown in Figure (1.8), which emphasize the various asphaltene hierarchical structures and shows how the hierarchical structures are very related in terms of structure and energies. The predominant asphaltene molecular architecture is shown in Figure (1.8),

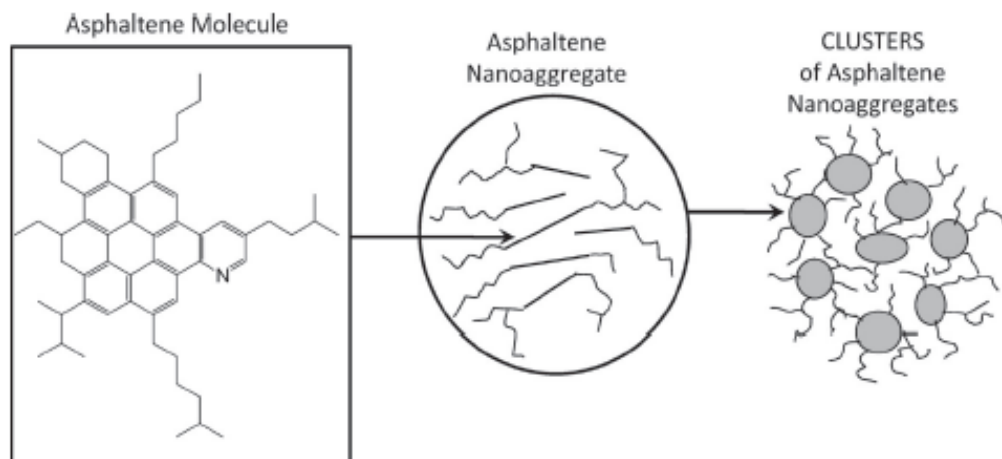


Figure 1.8: The Modified Yen model with its predominant asphaltene molecular hierarchy [31].

with its single, moderate-sized polycyclic aromatic hydrocarbon (PAH) ring system with peripheral alkane substituents.

These molecules can form asphalt nanoaggregates with a single, disordered stack of PAHs. The surface of the nanoaggregate is predominated by the alkane substituents. These nanoaggregates can form clusters of nanoaggregates. These asphaltene nanoaggregate clusters aren't much bigger than the nanoaggregates, and aggregate numbers are estimated to be eight nanoaggregates.

The prevailing but not only asphaltene molecular architecture, as shown in Figure (1.9), consists of a single, somewhat large (PAH) with cycloalkane, branched- and straight-series substituents. There is oftentimes heteroatom content; asphaltene nitrogen is completely contained within the PAH in pyrrolic structures and to a lesser extent pyridinic structures. Some sulfur is thiophene, therefore contained in the PAH, and the rather small oxygen content appears in various groups, with some probably phenolic.

The PAH is the essential site of intermolecular attraction. It is polarizable; thus,

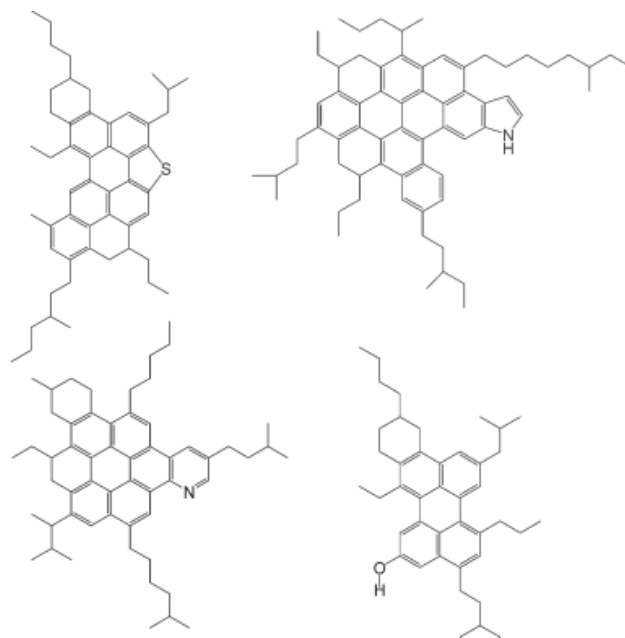


Figure 1.9: Proposed asphaltene molecular structures [31].

the PAH is the site of induced dipole and induced dipole interactions. In large measure, this interaction increases monotonically with the number of fused rings and thus is very important for the somewhat large PAHs of asphaltenes.

1.4 SAXS and SANS.

Small-angle X-ray scattering (SAXS) and small-angle X-ray neutron scattering (SANS) are predominantly used to detect particles in colloidal liquids. The diffusion centers in SAXS are localized fluctuations in electron intensity. Asphaltenes have a higher electronic intensity than their surrounding due to their polynuclear aromaticity, and so SAXS is useful for studying asphaltenes in their normal environment. The scattering centers in SANS are all nuclei, and so this technique has not been used to studying asphaltenes in their natural status. This technique is very useful for the studying of asphalt in solvents. It can increase the contrast between the asphaltenes and the

surrounding fluids by using perdeuterated solvents. Protons and Neutrons have significantly various scattering lengths. One then measures the localized fluctuations in deuteron density caused by the presence of the asphaltene particles in the perdeuterated solvent.

Chapter 2

Experimental

2.1 Setup Components.

The crystallite structure of asphalt can be determined by using XRD. For diffraction to occur in a crystal in which atoms were arrayed in the planes, the wavelength of the incident irradiation ought to be of the same order as the atomic space distances between crystallographic planes. Cross section of two X-rays of wavelength λ impinging at an angle θ on the surface of an asphalt cluster in which aromatic sheets are arrayed in planes separated by an interplanar distance d_M , as shown in figure (2.1) [25]. The planes with a relatively large number of atoms on them ordinarily give rise to strong reflection of the incident X-rays.

XRD supplies macrostructural information and the crystallite parameters of the molecules associated with the asphaltene aggregates. XRD grants quantitative density curves, and structural parameters can be obtained from the model and the position of the peaks (Trejo and other 2007) [26].

The X-ray densities measured through the range $2\theta = 3^\circ$ to 90° . The curves exhibit qualitatively similar peaks. Sideghi et al., (1986) [14], Siddiqui et al., (2002) [16], Yen et

by the following equation:

$$d_M = \frac{\lambda}{(2 \sin \theta)} \quad (2.2)$$

Where d_M is the interlayer distance, (λ) is the wavelength of the *CuK α* radiation and is Bragg's angle.

The distance between the saturated portions of the cluster was calculated according to the following equation:

$$d_\gamma = \frac{5\lambda}{(8 \sin \theta)} \quad (2.3)$$

The average height of the asphaltene cluster, L_c was calculated by using the Scherrer crystallite size equation, which $B_{\frac{1}{2}}$ the determination of full width at half maximum (FWHM) of the graphene band.

$$L_c = 0.9\omega \cos \theta = \frac{0.45}{B_{\frac{1}{2}}} \quad (2.4)$$

The average layer diameter of the aromatic sheets, can be calculated by the Scherrer's crystallite size:

$$L_a = \frac{1.84\lambda}{(\omega \cos \theta)} = \frac{0.92}{B_{\frac{1}{2}}} \quad (2.5)$$

Where $B_{\frac{1}{2}}$ is the full width at half maximum (FWHM) for the (11) band, and (ω) is the bandwidth.

The average number of aromatic sheets in a stacked cluster M_e , is given by values from the following equation:

$$M_e = \frac{L_c}{d_M} + 1 \quad (2.6)$$

2.2 Sample Preparation for XRD.

Asphalt binder samples were prepared as the thin film on glass slide holders by heating to 150° Celsius (C) around 10 minutes in a dry oven followed by removal and air refrigeration to room temperature. There are many ways to prepare the asphalt for XRD, as follows:

2.2.1 Method of Powder XRD.

Powder XRD is the most vastly used X-ray diffraction technicality for characterizing materials. As the sample is commonly in a powder form consisting of fine grains of single crystalline materials to research. The technique is as well used vastly for studying particles in liquid suspensions or polycrystalline solids of thin film materials.

The term powder means that the crystalline domains are randomly oriented in the sample. Moreover, when the 2-D diffraction pattern is recorded, it displays concentric rings of scattering peak corresponding to the various d spacing in the crystal lattice. The situations and the intensities of the peak are used for identifying the underlying build of the material.

Many studies have investigated the powder diffraction pattern arising from asphalt chemically precipitated from asphalt cement in both authentic and laboratory aged samples. These investigators calculated the structure parameters found in the asphalt samples related to the production of cross-sectional models using collected x-ray diffraction data before.

2.2.2 Method of Thin Film XRD.

There are a many exclusive discussions for using XRD to characterize thin film samples. Rising angular resolution is required because the peak from semiconductor materials

are sharp due to very low defect densities in the materials. Consequently, multiplied crystal monochromators are used to provide a highly collimated x-ray beam for these measurements. Before XRD each samples was placed on a glass slide and annealed in an oven at 150° Celsius (C) for 10 minutes in order to produce a flat film of about 1 mm thickness. X-ray diffraction spectral scans were obtained by Rigaku $D/Max - 2200v - PC$ using monochromatic ($Cu - k - \alpha$) radiation operating at 40 KV and 40 mA. The range of scanning used is 5° to $110^{\circ}2\theta$ at rate of $0.001^{\circ} 2\theta$ per second and detector count time of 5 seconds/step. The instrument is set up a divergence slit of 0.5° and receiving slit of 0.3mm [22].

The full width half maximum and profile fits were obtained by using a Pearson VII and Pseudo-Voigt with any background such as (Linear, Parabolic, Level, Fixed, 3rd Order polynomial, 4th order polynomial) over the range between 5° to 110° at 2θ . X-ray pattern creation and analysis was performed using a JadeTM version 6.1 software package incorporating Pearson VII and Pseudo-Voigt functions. The method for collected data was normalized to a common background to compare spectra features form the four main peaks that we measured, for example, (γ) , (11), (10), (002)_(graphene) [22, 23]. The specimen collected from specific location and Performance grade (PG) are illustrated in table (2.1) [23].

2.3 Spectral Line Shapes Modeled Using Mathematical Functions.

Segregation of the (γ) and (002) bands in the above manner to determine aromaticity, f , include three possible sources of errors. Fortunately, for some studies each of these could be dealt with in a reasonably satisfactory method.

Firstly, of these possible errors from small angle scattering which tends to increase

Asphalt Binder	Source	Modification Type	Grades
T1	Western	Timmins, Ontario	PG 64-34
T2	Canadian unknown	RET+PPA oxidized	PG 64-34
T3	unknown	SBS	PG 64-34
T4	unknown	SBS+acid-modified	PG 64-34
T5	unknown	SBS	PG 64-34
T6	unknown	oxidized	PG 64-34
T7	unknown	acid-modified(Lamont, Alberta)	PG 64-34
L1	Boundary Lake	oxidized	80/100 A,PG 58-22
L2	Montana/ Bow River	straight	150/200 B,PG 52-28
L3	Cold lake	straight	300/400 A, PG 46-34
L4	Redwater	straight	80/100 C, PG 58-22
L5	Loydminster	oxidized	20/100 A, PG 64-28
L6	Loydminster	straight	150/200 A, PG 52-34
L7	Cold lake	straight(Hearst, Ontario)	200/300 A, PG 52-34
H1	Loydminster	straight	150/200 A, PG 52-33
H2	Venezuelan	straight	150/200 B, PG 52-33
N1	unknown	straight(North Ontario)	PG 52-34
N2	unknown	straight	PG 52-34
N3	unknown	acid-modified	PG 52-34
E9	unknown	acid-modified various oxidized	PG 52-40
AAE	Loydminster	oxidized	60/70, PG 70-22
O1	unknown	oxidized	PG 52-34
O2	unknown	oxidized	PG 52-34

Table 2.1: Pertinent Asphalt Binder Properties [23]

the density on the low angle side of the (γ) band. For broad peaks scattering is hard to detect due to there being no discrete lines, i.e. only decreasing intensity with increasing angle. Assuming an approximately symmetrical (γ) band, it was potential to attribute some of the intensity on the low angle side of the band to small angle scattering and hence to exclude it from the calculation of f .

Secondly, the factor is that intensity of a (002) band due to a seven layered unit of approximately 2.4nm thickness, example, would exhibit an intensity 1.17 times that of the band for a two layered unit of approximately 0.7-1.1nm thickness. Thus, a variation in the size distribution of the repeat unit from sample to sample would result in an error in f . Fortunately, the asphalt under study has about the same L , and (FWHM) of the (γ) band, indicating a similar size allocation.

2.4 Pearson VII and Pseudo-Voigt.

Diffraction is more complete by using many various tools than decades ago both regarding instrumentation and particularly in data analysis. Numerous computer programs can give or solve almost any task, and the amount of information obtainable from a simple powder diffraction scan is very spectacular.

Hence, it is probable that line-broadening analysis will become a portion of monotone program output, together with line positions, lattice parameters, intensities, etc. Pattern analysis software, such as in some retrieved refinement program, already includes refinable parameters corresponding to domain size and strain. Regrettably, inspection of line broadening is rarely a standard procedure. Being so automated, the line-broadening analysis is very often inexact, because the models used inappropriately in the most retrieved program.

The Voigt function form has been the foundation most quantitative analysis of

x-ray diffraction (XPD) spectra. Unfortunately, a true analysis form the detour of a Gaussian and Lorentzian ($G * L$) is not available and so workable systems have adopted two approximations to the real Voigt function.

Gaussian and Lorentzian Product form:

$$GL(x, m, F, E) = \frac{\exp(-4 \ln 2 (1 - m) \frac{(x-E)^2}{F^2})}{1 + 4m \frac{(x-E)^2}{F^2}} \quad (2.7)$$

Gaussian and Lorentzian Sum form:

$$SGL(x, m, F, E) = (1 - m) \exp(-4 \ln 2 (1 - m) \frac{(x-E)^2}{F^2}) + \frac{m}{1 + 4 \frac{(x-E)^2}{F^2}} \quad (2.8)$$

2.5 Generalized Fermi Function Applied to the Experimental X-Ray Line Profile Analysis.

The Generalized Fermi function (GFF) is a simple function with a minimal number of parameters, suitable for minimization methods. It is defined by the relation:

$$h_S = \frac{A}{e^{-a(s-c)} + e^{b(s-c)}} \quad (2.9)$$

Where A, a, b, c are unknown parameters and $s = 2 \frac{\sin \theta}{\lambda}$. The values A and c describe the amplitude and the position of the peak, a and b control shape of the peak. GFF has been used by Mathematica software and is employed to fit raw data from XRD on the Generalized Fermi Function.

2.6 Exponential Asymmetric Blend Based upon Voigt-type Line-Shapes.

Given either of the above Gaussian / Lorentzian asymmetric line-shapes, an asymmetric profile is obtained from a mix function as follows:

$$Y(x) = GL(x) + (1 - GL) * T(x) \quad (2.10)$$

Where,

$$T(x, k, F, E) = \exp\left(-k \frac{(x - E)}{F}\right) \quad (2.11)$$

if $x \leq E$ Otherwise

2.7 Line Shapes Analysis Using Peak Search and Profile Fit.

The XRD spectra were peak searched using a parabolic filter (screened out $k\alpha - 2$ peaks, range between 5° to 35° , threshold sigma 2.5, intensity cutoff 0.1 percent, range to find background 1.0, peak location summit, points to average background 7) over the angular range from 5° to 110° .

The full width half maximum (FWHM) and profile fits were gained by using either Pearson VII and Pseudo-Voigt function (parabolic background, Exponent 1.5, Lorentzian 0.5, Skewness 0.0) over the range 5° to 35° , and 60° to 110° at 2θ on the XRD line spectra of interest. The XRD spectra were also modeled in Mathematica using GFF.

Chapter 3

Results and Discussion.

These XRD patterns consist of the four major peaks in asphaltene (11),(10),(γ),(002), as depict in the Yen model [5], and shown in figure (1.7). There are also peaks in some samples as we can see these (L1, L2, L4, T1, T2, H1, N1, O1, E9) due to additional chemical phases such as paraffins wax, and other impurities.

If we consider the table below (3.1) we can observe different aromaticity and crystallite values for the three functions (Pearson VII, Pseudo-Voigt, GFF). If we take into account the values of (Pearson VII, Pseudo-Voigt), we found the values are similar to some extent. Where the values at f_a ranging between 0.4 to 0.7 , $d_M = 4.1$ to 4.6 , $d_\gamma = 5.1$ to 6.1 , $L_c = 3.7$ to 8.2 , $L_a = 3.2$ to 8.4 , and $M_e = 1.8$ to 3.0 .

Additionally, we will note the data that indicates GFF values range from $f_a = 0.5$ to 0.9 , $d_M = 4.4$ to 7.7 , $d_\gamma = 5.5$ to 6.5 , $L_c = 2.4$ to 5.9 , $L_a = 2.6$ to 6.6 , and $M_e = 1.5$ to 2.3 .

Through the results shown in the table, we can consider that the profile fitting in (GFF) is less consistent than that for (Pearson-VII and Pseudo-Voigt), due to the asymmetry of the XRD patterns. Hence , GFF is more sensitive to asymmetry and has consequence in lower and higher values of f_a , d_M , d_γ , L_c , L_a , and M_e .

Sample	f_a			d_M			d_γ			L_C			L_a			M_e		
	P	V	GF	P	V	GF	P	V	GF	P	V	GF	P	V	GF	P	V	GF
L1	0.54	0.35	0.76	4.3	4.3	7.7	5.3	5.3	5.5	6.3	6.2	5.7	3.4	3.4	2.8	2.5	2.4	2.0
L2	0.44	0.46	0.91	4.4	4.4	4.5	5.5	5.5	5.7	6.4	5.4	5.6	7.6	7.6	2.7	2.5	2.2	2.2
L3	0.51	0.54	0.75	4.4	4.4	4.4	5.5	5.5	5.6	3.5	4.5	5.9	5.4	5.4	2.8	1.8	2.0	2.3
L4	0.41	0.45	0.97	4.8	4.8	5.1	5.9	5.9	6.3	6.4	6.4	5.6	7.7	7.7	2.8	2.3	2.3	2.1
L5	0.45	0.55	1.0	4.8	4.8	4.7	6.1	6.1	5.8	6.2	6.2	5.9	8.4	8.4	2.8	2.3	2.3	2.2
L6	0.46	0.50	0.83	4.2	4.2	4.7	5.3	5.3	5.8	6.1	5.2	5.7	4.1	4.1	2.9	2.5	2.2	2.2
L7	0.60	0.72	0.86	4.3	4.3	5.5	5.5	5.5	6.7	3.7	4.7	5.4	5.6	5.6	2.6	1.9	2.1	1.8
T1	0.45	0.55	0.84	4.4	4.4	4.9	5.4	5.4	6.1	6.4	6.4	2.7	6.7	6.7	5.5	2.5	2.4	1.5
T2	0.53	0.66	0.83	4.1	4.1	4.7	5.1	5.1	5.8	6.3	6.3	2.7	5.7	5.7	5.6	2.5	2.5	1.6
T3	0.53	0.61	0.76	4.1	4.1	5.1	5.1	5.1	6.1	6.3	6.3	2.8	7.6	7.6	5.8	2.5	2.5	1.5
T4	0.55	0.69	0.50	4.3	4.3	5.2	5.4	5.4	6.5	4.3	5.3	2.7	7.7	7.7	5.6	2.0	2.2	1.5
T5	0.50	0.55	0.73	4.4	4.4	4.8	5.4	5.4	6.0	6.4	6.4	2.8	7.1	7.1	5.7	2.5	2.4	1.6
T6	0.66	0.71	0.93	4.4	4.4	5.2	5.5	5.5	6.3	5.6	5.6	2.7	5.7	5.7	5.6	2.3	2.3	1.5
T7	0.54	0.55	0.93	4.3	4.3	4.7	5.3	5.3	5.8	4.4	3.4	2.6	7.7	7.7	5.4	2.0	1.8	1.5
N1	0.51	0.52	0.94	4.2	4.2	5.2	5.3	5.3	6.5	5.6	6.6	2.6	4.3	4.3	5.3	2.3	2.6	1.5
N2	0.46	0.52	0.75	4.6	4.6	4.7	6.0	6.0	5.8	5.4	5.4	2.8	4.2	4.2	6.0	2.6	2.1	1.6
N3	0.45	0.44	0.52	4.2	4.2	4.9	5.1	5.1	6.2	7.5	7.5	2.8	4.6	4.6	6.6	2.3	2.8	1.5
H1	0.54	0.52	0.73	4.1	4.1	4.7	5.1	5.1	5.8	6.7	6.7	2.6	4.4	4.4	5.3	2.6	2.6	1.6
H2	0.44	0.44	0.87	4.5	4.5	4.9	5.4	5.4	6.2	6.2	7.1	2.9	5.2	5.1	5.5	2.4	2.6	1.6
O1	0.48	0.54	0.56	4.6	4.6	4.9	6.0	6.0	6.2	6.4	6.4	2.4	3.2	3.2	5.0	2.4	2.4	1.5
O2	0.48	0.53	0.81	4.1	4.1	4.4	5.1	5.1	5.5	4.5	6.5	2.8	5.1	5.1	6.0	2.1	2.6	1.6
AAE	0.51	0.54	0.61	4.4	4.4	4.9	5.5	5.5	6.2	3.7	4.7	2.7	7.3	7.3	5.5	2.0	2.0	1.5
E9	0.53	0.55	0.81	4.1	4.1	4.7	5.1	5.1	5.8	8.2	5.2	2.7	4.1	4.1	5.6	3.0	2.2	1.6

Table 3.1: Aromaticity and Crystallite Parameters for Asphalt Binder Samples Calculated Using Pearson-VII(P), Pseudo-Voigt(V), and Generalized Fermi (GF) Function.

3.1 X-ray Diffraction Patterns.

XRD patterns generated for the 23 different asphaltene specimens were generated by standard processes as described in the JadeTM software (version 6.1) and experimental. The below figures from (3.1) to (3.12) illustrate types of the asphalt samples(L1-L7, T1-T7, N1-N3 ,H1, H2, O1, O2, AAE, E9).

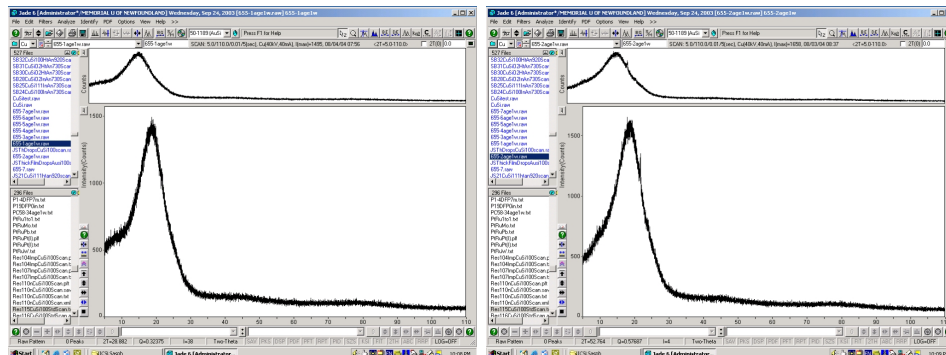


Figure 3.1: Paradigms T1 and T2 for the XRD profile

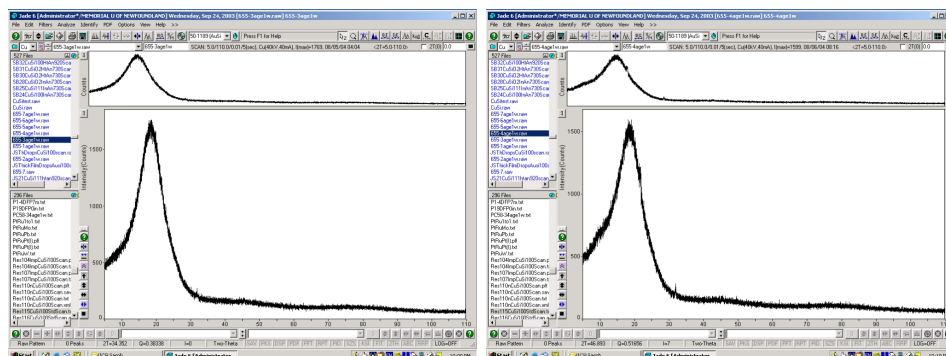


Figure 3.2: Paradigms T3 and T4 for the XRD profile

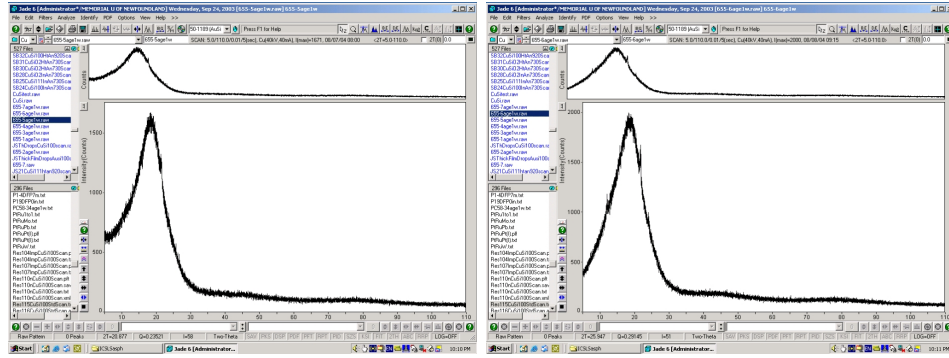


Figure 3.3: Paradigms T5 and T6 for the XRD profile

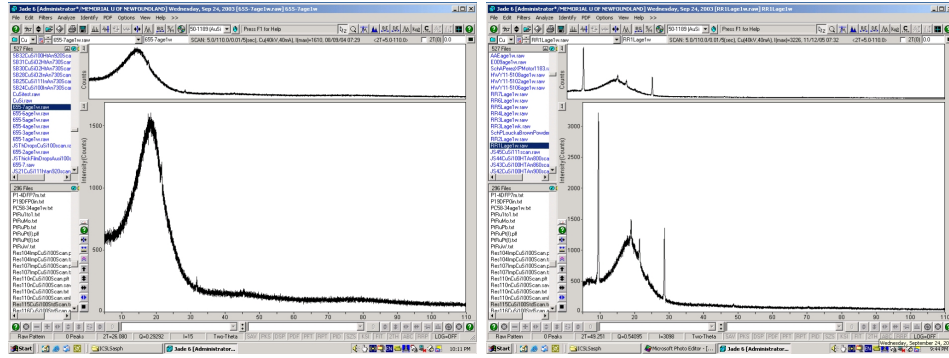


Figure 3.4: Paradigms T7 and L1 for the XRD profile

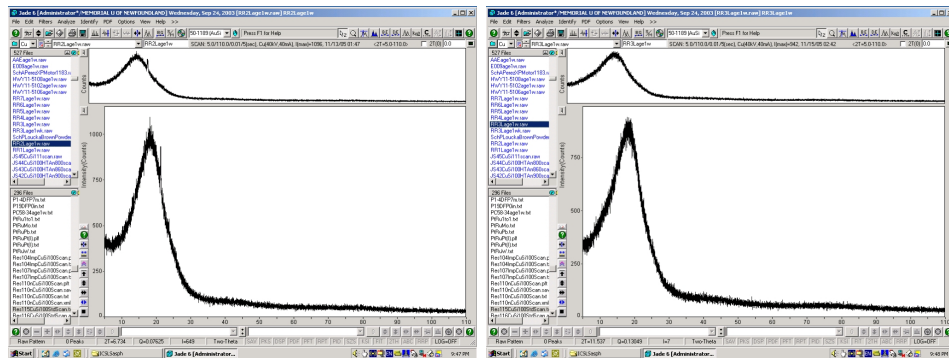


Figure 3.5: Paradigms L2 and L3 for the XRD profile

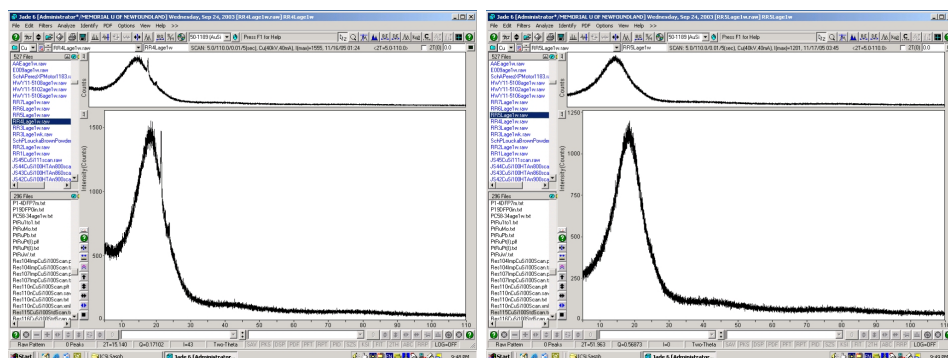


Figure 3.6: Paradigms L4 and L5 for the XRD profile

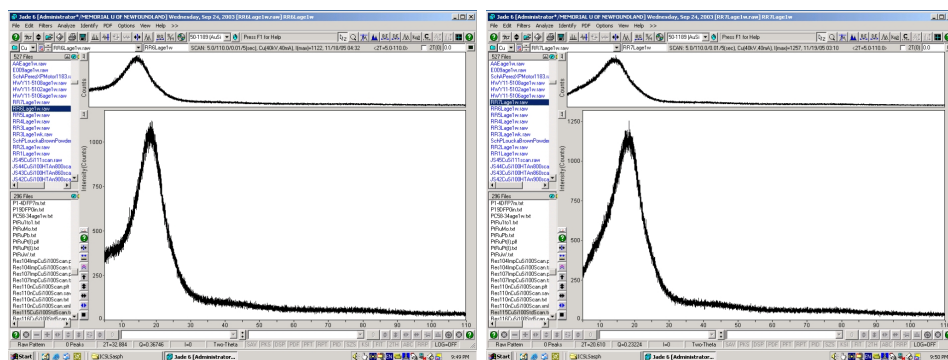


Figure 3.7: Paradigms L6 and L7 for the XRD profile

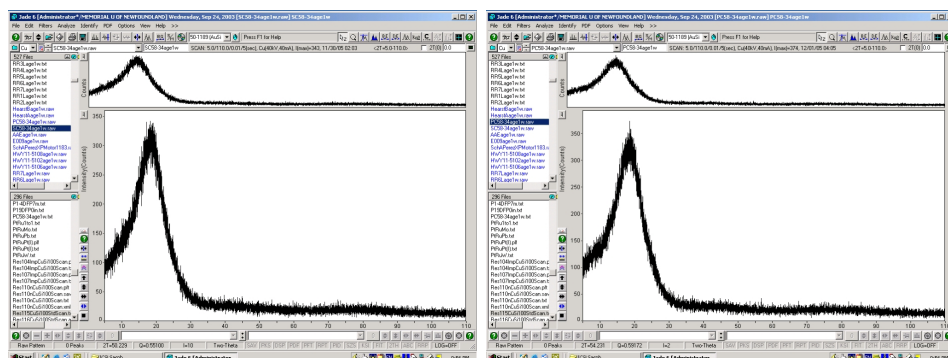


Figure 3.8: Paradigms O1 and O2 for the XRD profile

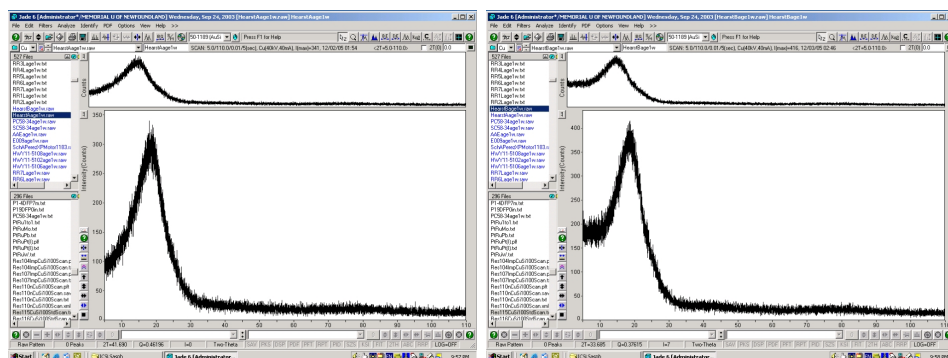


Figure 3.9: Paradigms H1 and H2 for the XRD profile

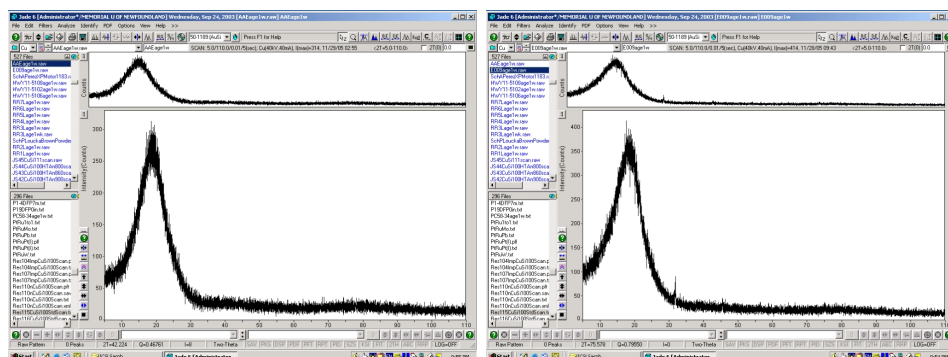


Figure 3.10: Paradigms AEE and E9 for the XRD profile

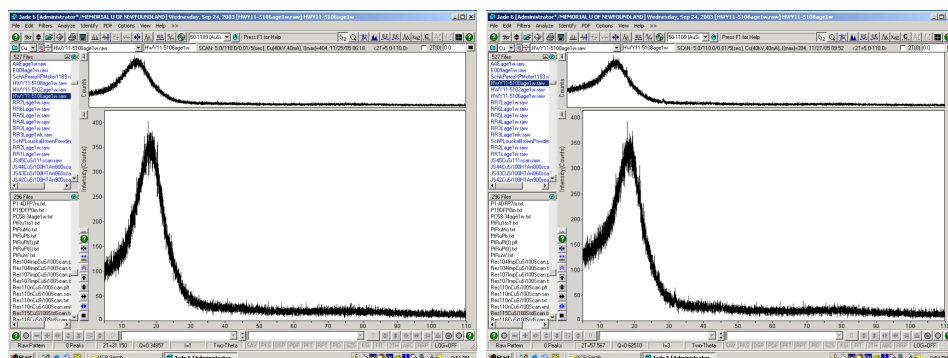


Figure 3.11: Paradigms N1 and N2 for the XRD profile

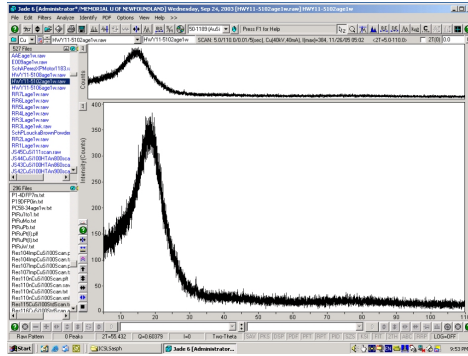


Figure 3.12: Paradigms N3 for the XRD profile

3.2 XRD Peak Search and Peak Profile Fitting.

X-ray pattern analysis is necessary to get the best optimum peak. This includes accomplishing several procedures in the correct order and with some experiments. First, operation for the peak search, which identifies the importance peak in the profile apart background irradiation and any noise. The recommended proceedings encompass using one of the preferable backgrounds such as (Linear, Parabolic, 3rd order Polynomial, 4th order Polynomial). Selecting the raw data point at 99, examination out ($K_a - 2$) peaks, threshold sigma at (2.5), range between ($5^\circ - 35^\circ$), intensity cutoff (0.1)%, range to find background (1.0), exponent (1.5), Lorentzian (0.5), skewness (0.0).

Automatically, the peak search is commonly very sensitive enough to generate a report that is listing all probable peaks. Any other peaks that are not needed can be omitted through the report. For the remaining peaks and their places, the supplemental analysis is required by performing the peak profile fitting including the full width at half maximum (FWHM). This is achieved by opting from Mathematical functions (GFF, Pearson VII, Pseudo-Voigt) using (Linear, Parabolic, 3rd order Polynomial, 4th order Polynomial) over the range between ($5^\circ - 35^\circ$) 2θ on the XRD line.

3.3 Influence of Peak Shape Functions.

The XRD peak profile fitting functions of Pearson VII and Pseudo-Voigt have various peak shapes. Pearson VII is an exponential blending of Gaussian and Lorentzian. The Pseudo-Voigt shape is a linear combination of Gaussian and Lorentzian components. Empirical peak shape functions (y) and the GFF are expressed Mathematically as follows:

Gauss

$$y(x) = G(x) = \frac{C_G^{1/2}}{(\sqrt{\pi}H)} \exp(-C_G x^2) \quad (3.1)$$

Lorentzian

$$y(x) = L(x) = \frac{C_L^{1/2}}{(\pi H')} (1 + C_L x^2)^{-1} \quad (3.2)$$

Pearson VII

$$y(x) = PVII(x) = \frac{\Gamma(\beta)}{\Gamma(\beta - 1/2)} \frac{C_P^{1/2}}{(\sqrt{\pi}H)} (1 + C_P x^2)^{-\beta} \quad (3.3)$$

Pseudo-Voigt

$$y(x) = PV(x) = \eta \frac{C_G^{1/2}}{(\sqrt{\pi}H)} \exp(-C_G x^2) + (1 - \eta) \frac{C_L^{1/2}}{(\pi H')} (1 + C_L x^2)^{-1} \quad (3.4)$$

Generalized Fermi Function

$$y(x) = \frac{A}{e^{-a(s-c)} + e^{b(s-c)}} \quad (3.5)$$

Where A , a , b , c are unknown parameters and $s = 2 \frac{\sin \theta}{\lambda}$.

The values A and c describe the amplitude and the position of the peak, a and b control shape of the peak. GFF has been used by Mathematica software and employed to fit raw data from XRD on the Generalized Fermi Function.

C_G , is the normalization factor for the Gauss function.

C_L , is the normalization factor for the Lorentz function.

C_P , is the normalization factor for the Pearson VII function.

H and H' are full width at half maximum (FWHM).

$$H = (U \tan^2 \theta + V \tan \theta + W)^{1/2} \quad (3.6)$$

It is the (FWHM) as a function of θ for Gauss, Pearson VII, Pseudo-Voigt functions. U , V and W are free variables [34].

$$H' = \frac{U}{\cos \theta} + V \tan \theta \quad (3.7)$$

It is the (FWHM) as a function of θ for Lorentz functions. U and V are free variables.

$$(x) = \frac{2\theta_i - 2\theta_k}{H_k} \quad (3.8)$$

Where (x) is the XRD Bragg angle of the i^{th} point in the diffraction pattern with its origin in the position of k^{th} peak divided by the peak's FWHM.

$(2\theta_i)$, is the Bragg angle of the i^{th} point of the diffraction pattern.

$(2\theta_k)$, is the Bragg angle of the k^{th} Bragg reflection [34–36].

$$(\eta) = \eta_o + \eta_1 2\theta + \eta_2 \theta^2 \quad (3.9)$$

Where η is the Pseudo-Voigt function. η_o , η_1 and η_2 are free variables. Γ is the gamma function.

$$(\beta) = \beta_o + \frac{\beta_1 - 2\theta}{+} \frac{\beta_2}{(2\theta)^2} \quad (3.10)$$

Where β is the exponent as a function of Bragg angle in the Pearson VII function, and β_o , β_1 and β_2 are free variables.

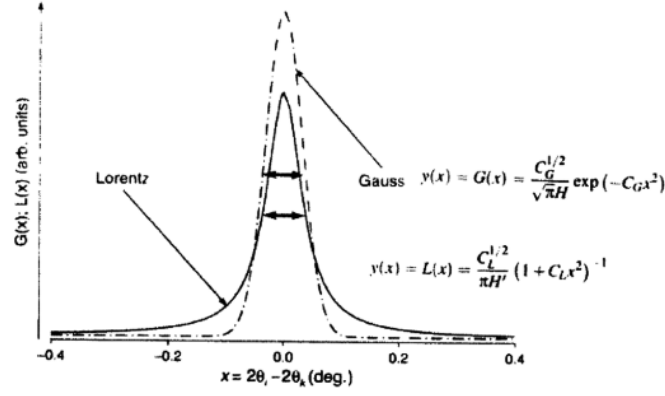


Figure 3.13: Gauss and Lorentz peak shape function [34].

The figure (3.13) illustrate the peak shape functions and describe a Gauss function that is longer at the top with little to no side tails at the bottom relative to the Lorentz that is a shorter sharp top with tall tails at the bottom.

Gauss and Lorentz functions are symmetrical $G(x) = G(-x)$ and $L(x) = L(-x)$. The models of shapes at Bragg peaks, which are the consequence of convoluting multiple instruments and sample function are scarcely described well in XRD by simple Gauss or Lorentz distribution, specially in x-ray diffraction. Commonly empirical peak shapes have located some place between the Gauss and Lorentz distributions and they can be better represented as the admixture of the two functions. These two functions can be convoluted in various ratios; however, this is unsuitable since it requires numeral integration while peak shape function parameters change.

The Gauss and Lorentz compound are mixed in η to $1 - \eta$ proportion, so that the value of the mixing parameter varies from 0 Lorentz to 1 Gauss. It is comparable to Lorentz distribution expect the exponent (β) differ in the Pearson VII, while it remains constant ($\beta=1.5$) in the Lorentz function. Pearson VII supply an intensity distribution nearby the Pseudo-Voigt function where the exponent ($\beta=1.5$) it is analogous to the Lorentz distribution, and when $\beta \cong 10$, Pearson VII become equivalent to of Gaussian function. However, if the exponent for the range between $0.5 < \beta < 1$ or $\beta > 10$, the

peak shape extends beyond Gauss or Lorenz functions, respectively, but values of β are rarely observed in practice.

Pearson VII and Pseudo-Voigt functions are symmetrical, so values of (x) , for all four experimental functions, establishes the location of peak extreme, that is observed when:

$$x = 0 \text{ and } 2\theta_i = 2\theta_k$$

Then, in the general situation the peak full width at half maximum (FWHM) at a particular 2θ angle is illustrated as the following equation:

$$FWHM = H = \sqrt{U \tan^2 \theta + V \tan \theta + W} \quad (3.11)$$

Where the

FWHM term, H , is a component of Pearson VII and Pseudo-Voigt functions.

FWHM is correlate to crystallite size and microstrain.

U is the parameter most strongly associated with strain broadening.

The later varies with 2θ and its reliance on the Bragg's angle is most commonly represented by experimental peak broadening function, that contains three free parameters U , V , and W (exception for the Lorentzian, which general has two free variables).

3.4 XRD types with Different Backgrounds and Effect of Backgrounds.

We will discussion the three different types of samples and conducting experiments fitting to obtain the best peaks, we initially to use all backgrounds such as (Fixed, Level, Linear, Parabolic, 3^{rd} order, 4^{th} order). The samples which we worked on are (T1, T3, T5).

Through numerous experiments in the x-ray, we found that the best backgrounds we used are (Linear, Parabolic, 3^{rd} order, 4^{th} order), because they are giving the obvious peaks for the (γ) and $(002)_{graphene}$. These are shown in figures (3.14 - 3.16).

If we look at the following table (3.2), we will note that the percent of error for the parameters ranging between 5.0 and 32.3, where the highest value is 32.3 at 3^{rd} , and less value is 5.0 at 4^{th} order, for each of the Pearson VII, Pseudo-Voigt. At different angles between 19.7° and 22.5° .

If we take, as an example, T3 at Pearson VII, we can see it has a lower residual of error, in contrast T5 at Pearson VII it has the highest value in the error rate. Also, T3 at Pseudo-Voigt, we can see it has a lower residual of error, in contrast T5 at Pseudo-Voigt it has the highest value in the error rate.

Table (3.3) shows the convergent values despite differing backgrounds. If we consider values d_M , d_γ , L_C , L_a and M_e , we found that they are very close to a great extent, and this demonstrates that the backgrounds are delicate and sensitive.

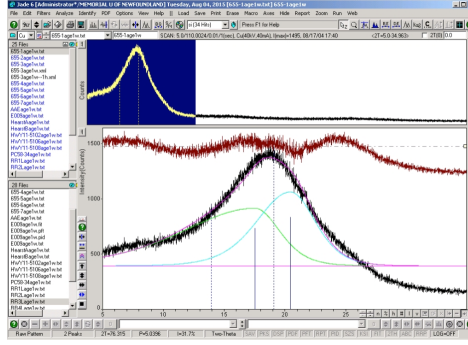


Figure 3.14: Samples T1 for the best peak.

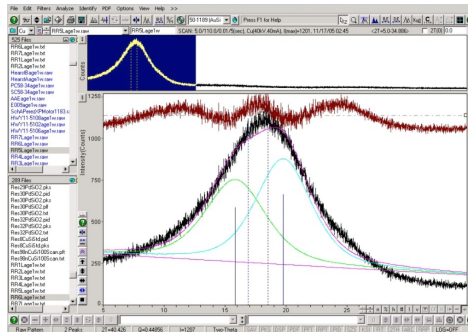


Figure 3.15: Samples T3 for the best peak.

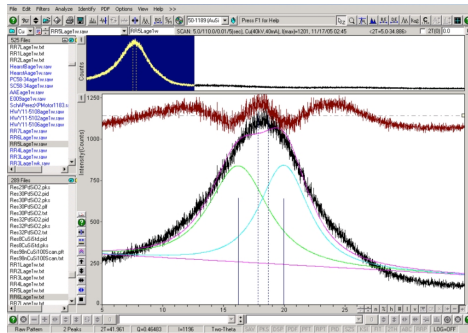


Figure 3.16: Samples T5 for the best peak.

Samples	Profile	Background	Residual Error of fit %	2θ
T1	Pearson- VII	Linear	8.7	19.8
		Parabolic	8.7	20.4
		3^{rd} order	32.3	20.4
		4^{th} order	6.2	20.1
T3	Pearson- VII	Linear	6.4	21.1
		Parabolic	6.6	19.7
		3^{rd} order	6.5	19.7
		4^{th} order	5.6	20.4
T5	Pearson- VII	Linear	14.2	22.5
		Parabolic	15.3	21.2
		3^{rd} order	8.6	19.6
		4^{th} order	7.1	19.7
T1	Pseudo-Voigt	Linear	8.1	21.2
		Parabolic	8.7	19.7
		3^{rd} order	6.9	19.7
		4^{th} order	26.6	20.4
T3	Pseudo-Voigt	Linear	6.5	22.1
		Parabolic	6.3	20.6
		3^{rd} order	8.4	22.1
		4^{th} order	5.0	21.8
T5	Pseudo-Voigt	Linear	13.8	21.2
		Parabolic	14.5	21.6
		3^{rd} order	8.1	20.6
		4^{th} order	8.2	20.4

Table 3.2: The Effect of Background on fit

Sample	Background	f_a			d_M			d_γ			L_C			L_a			M_e		
		P	V	GF	P	V	GF	P	V	GF	P	V	GF	P	V	GF	P	V	GF
T1	Linear	0.9	0.9	0.8	4	4	5	5	5	6	4	4	4	6	7	6	2	2	1.8
	Parabolic	0.4	0.4	0.8	4	4	5	5	5	6	4	4	4	6	7	6	2	2	1.8
	3 rd order	0.4	0.8	0.8	4	4	5	5	5	6	4	4	4	6	7	6	2	2	1.8
	4 th order	0.5	0.4	0.8	4	4	5	5	5	6	4	4	4	7	7	6	2	2	1.8
T3	Linear	0.2	0.2	0.7	4	4	5	4	5	6	4	5	4	7	7	6	2	2	1.8
	Parabolic	0.4	0.3	0.7	4	4	5	5	5	6	4	6	4	7	7	6	2	2	1.8
	3 rd order	0.4	0.2	0.7	4	4	5	5	5	6	4	6	4	7	8	6	2	2	1.8
	4 th order	0.4	0.2	0.7	4	4	5	5	4	6	4	5	4	7	8	6	2	2	1.8
T5	Linear	0.4	0.6	0.7	4	4	5	5	5	5	4	4	4	7	8	6	2	2	1.8
	Parabolic	0.5	0.7	0.7	4	4	5	5	5	6	4	4	4	6	7	6	2	2	1.8
	3 rd order	0.5	0.6	0.7	4	4	5	5	5	6	4	4	4	6	7	6	2	2	1.8
	4 th order	0.5	0.6	0.7	4	4	5	5	5	6	4	4	4	6	7	6	2	2	1.8

Table 3.3: Aromaticity and crystallite size for three samples, four backgrounds using Pearson-VII(P), Pseudo-Voigt(V), and Generalized Fermi Function(GFF).

3.5 Spectral Line Shapes Analysis.

XRD profile fits include (Pearson VII,Pseudo-Voigt, and GFF) emulation results.

3.5.1 Samples figures with GFF.

The following figures from (3.17) to (3.36) illustrate the 20 samples (T1 to T7, L2 to L7, N1 to N3, H1, H2, O1, O2, E9) of the GFF profile fits from XRD data are shown below.

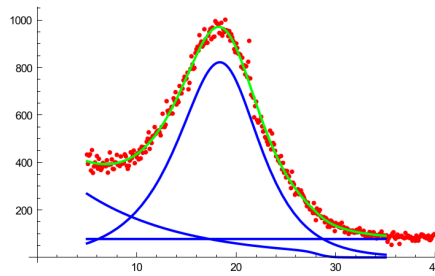


Figure 3.17: Samples L2 for the GFF profile

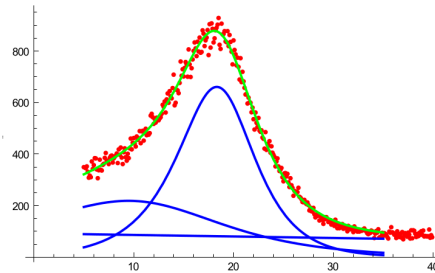


Figure 3.18: Samples L3 for the GFF profile

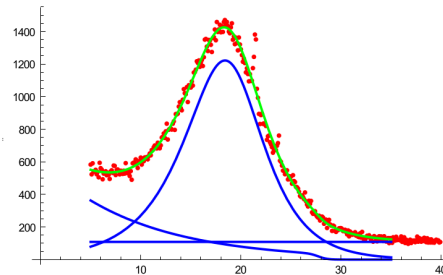


Figure 3.19: Samples L4 for the GFF profile

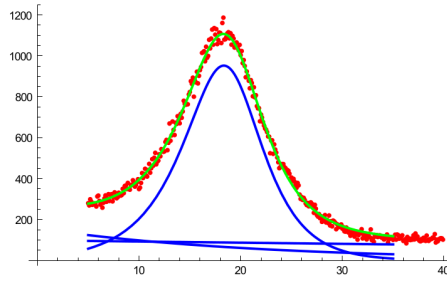


Figure 3.20: Samples L5 for the GFF profile

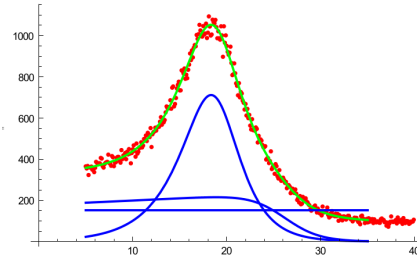


Figure 3.21: Samples L6 for the GFF profile

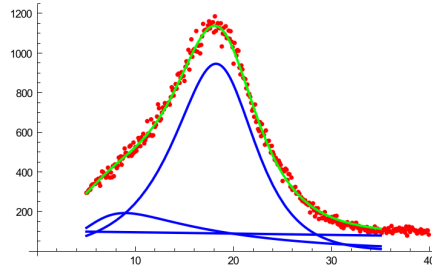


Figure 3.22: Samples L7 for the GFF profile

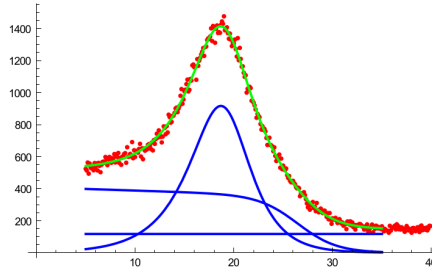


Figure 3.23: Samples T1 for the GFF profile

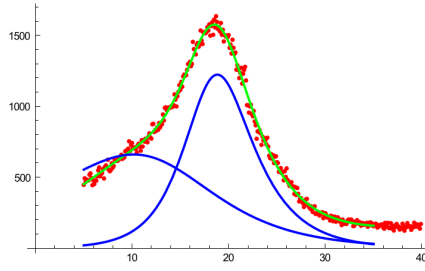


Figure 3.24: Samples T2 for the GFF profile

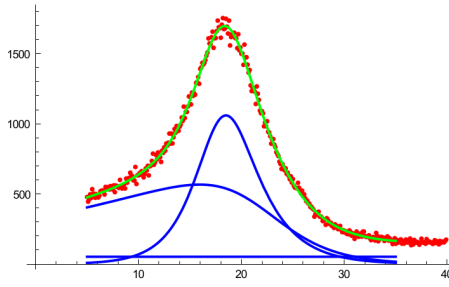


Figure 3.25: Samples T3 for the GFF profile

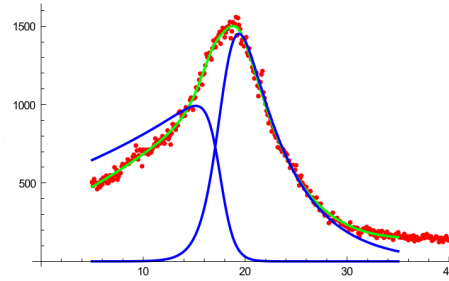


Figure 3.26: Samples T4 for the GFF profile

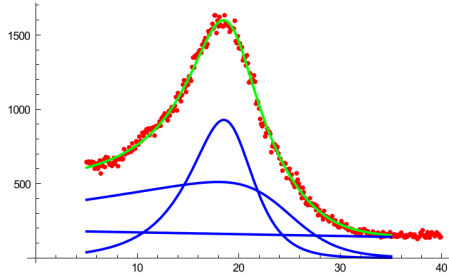


Figure 3.27: Samples T5 for the GFF profile

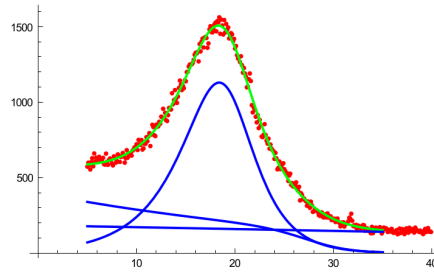


Figure 3.28: Samples T7 for the GFF profile

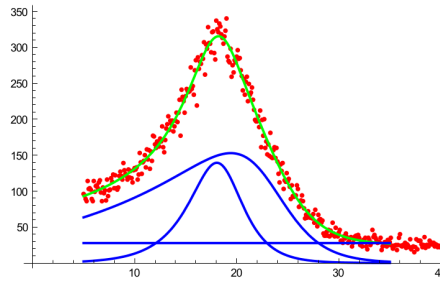


Figure 3.29: Samples O1 for the GFF profile

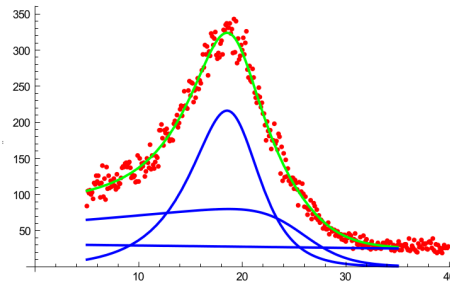


Figure 3.30: Samples O2 for the GFF profile

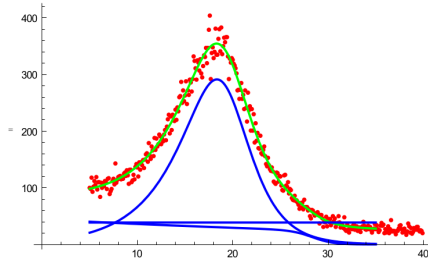


Figure 3.31: Samples N1 for the GFF profile

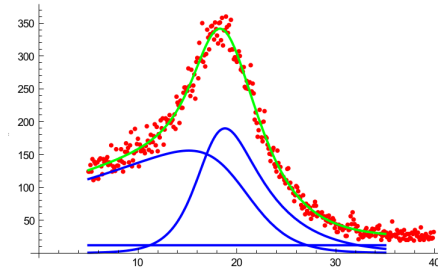


Figure 3.32: Samples N2 for the GFF profile

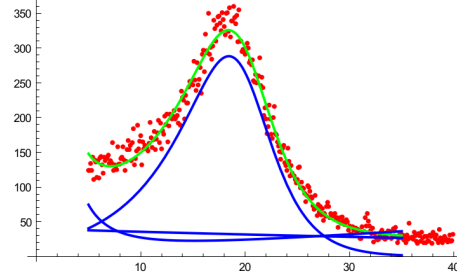


Figure 3.33: Samples N3 for the GFF profile

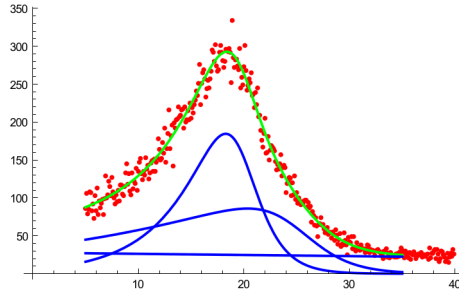


Figure 3.34: Samples H1 for the GFF profile

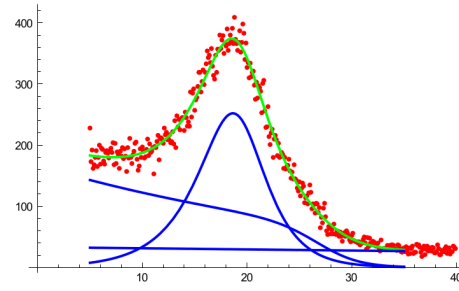


Figure 3.35: Samples H2 for the GFF profile

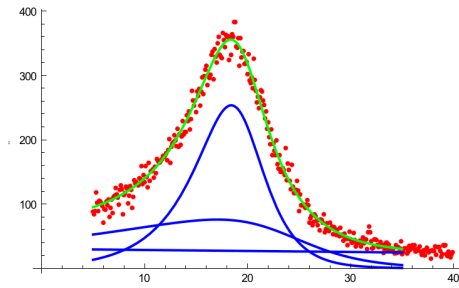


Figure 3.36: Samples E9 for the GFF profile

3.6 Comparing of XRD Results for Asphalt.

The X-ray diffraction patterns impose fitting of the impractical distributions which are crucial to getting information from the spectral lines. Pearson VII and Pseudo-Voigt fitting procedure are used, and the three most important bands (γ), (002) and (10) positioned at approximately $2\theta = 19^\circ, 23^\circ$, were used as the primary assessments. Backgrounds are an essential case in the XRD patterns of asphaltene binder.

On the high 2θ side of the (10) peak, the (002) band may be observed in some situations at 2θ at approximately around 22.5° . As well, estimation of the peak width and density were needed to initiate the regression analysis. On the other hand, on the low 2θ side the baseline is not sufficiently well defined. So, one ought to use the high-value end of the XRD pattern and fix this as a steady baseline. This introduces the possibility for a sensible assumption, inspired assumption, of statistical inaccuracies that may impact the result for the operator.

Aromaticity (f_a) of approximately values 0.50 for T4 and 1.0 for L5 using GFF shows that the data fits were found to be very weak. T4 has a lower value, and L5 has the highest value in GFF function. For example, asphalt T4 form the presence of the XRD profile, as apparently having a large (002) contribution. Nevertheless, when we were using GFF the peak become very wide, and hence the (002) contribution become very small, making the aromaticity in the amount of only 0.50, while the Pseudo-Voigt and Pearson VII gave consistent aromaticity of approximately 0.55 and 0.69 respectively.

The same situation, when we see asphalt N3, having an f_a of about 0.52 when fitted in GFF, and 0.45 and 0.44 are obtained when we were using the same proceedings for Pearson VII and Pseudo-Voigt functions. Some of the data have the same result an f_a such as L1, T3 they get the value 0.76, and T6, T7 they were having 0.93. On the other side, samples T1 to T7 have convergent values somewhat for Pearson VII and

Pseudo-Voigt calculation at f_a .

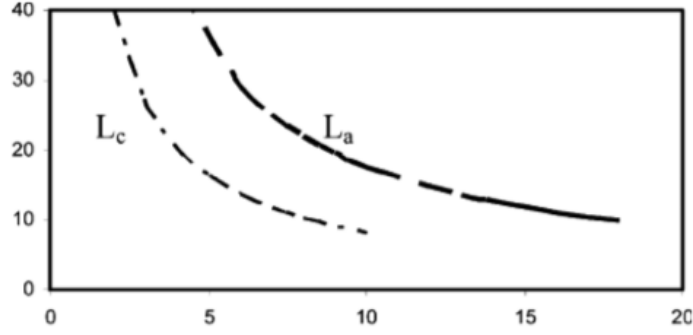


Figure 3.37: Relationship between crystalline L_a and L_c for full width at half maximum (FWHM) [38].

The crystallite parameter of the interlayer distance has extremely high values of L_c from GFF compared to Pearson VII Pseudo-Voigt. However, the rest of the result for all samples are proportionate. The two crucial parameters to understand crystallite are L_a and L_c . These are very sensitive and to full width at half maximum (FWHM), as shown in figure (3.37), where the relationship between L_a and L_c the theoretical calculation. It is obvious that, L_c is sensitive to small changes in γ , i.e., a change from $2\theta = 5^\circ$ to 6° cause the stack height to lessening from 3.0 to 1.5 nm. The sheet diameter data are less sensitive and remain almost fixed around 1.1 to 1.5nm. For the narrow (10) band will very impact significantly. We will realize that the basic result various with directions and when changing from Pearson VII to Pseudo-Voigt in XRD. The fitting processes may indeed be oversimplified in that graphene usually include a formation of non-symmetric (002) peak formed by diverse contributions, such as the noise in the residue of error for the data.

Chapter 4

Conclusions

XRD patterns were profile fitting by three major functions, Pearson VII, Pseudo-Voigt and Generalized Fermi function (GFF). For the Pearson VII and Pseudo-Voigt using JadaTM software samples were compared for aromaticity and crystallite size with different values. Also, a generalized Fermi modeled the XRD data in Mathematica with mixed results relative to Pearson VII, Pseudo-Voigt functions.

Asphaltene from twenty-three samples were prepared various provenance and analyzed by XRD (Pearson VII, Pseudo-Voigt) as raw data and by GFF modeling. Aging operations for all asphalt binder samples increased, over a period, and the peaks were analyzed and marked. It was found that the crystallinity increases with increasing exposure of asphalt with aging. For a minute change in the angles of the profiles shows a change of planes of the atoms, and the consequence showed a correlation through Pearson VII, Pseudo-Voigt and GFF.

XRD experimental reveal some features of asphalt aggregates. The mass of connected asphalt molecules with stacked aromatic sheet, are comparatively stable up to 150°C ,and the layer distance between aromatic sheets and the number of aromatic sheet in a stacking cluster are regular in three asphalt types. Analysis of the re-

sult procured in this work indicates that the XRD provides insight on the structural and compositional properties of asphalt binder and knowledge of natural and artificial sources of asphalt binder, which are important to understanding the aging of asphalt binder and pavement.

Chapter 5

Recommendations for Future Work

Develop an understanding of asphalt binder types and pavement layer bonding. Also, understanding the Physical and Chemical structure for both asphalt and pavement. Develop protocols for obtaining optimum peaks when using the JadeTM software. Analyze different parameters and various backgrounds. Change the values for the parameters such as (Threshold sigma, Range between $(5^{\circ} - 110^{\circ})$, Intensity cutoff, Range to find background, Exponent, Lorentzian, Skewness).

Develop commingle designing for high modulus asphalt mixes, including the selection of binder, optimum asphalt content for low voids.

Using Mathematica for different background functions.

Chapter 6

Appendices

6.1 Proceedings for Profile Fitting a Diffraction Patterns.

1. Open the XRD model.
 2. Overlay PDF reference for the sample.
 3. Zoom in on the first peak to analyze.
 - try to zoom in on only one peak.
 - and be sure to include some background on either side of the peak.
 4. Open profile fitting dialogue to configure parameter.
 5. Refine the profile fit for the first peak.
 6. Review quality of profile is fitting.
 7. Move to next peak(s).
 8. Continue to the entire pattern is fit.

6.2 GFF routine using Mathematica.

The following explanation illustrated some of the proceedings when we used Mathematica program to get the evident peak and accurate result.

```

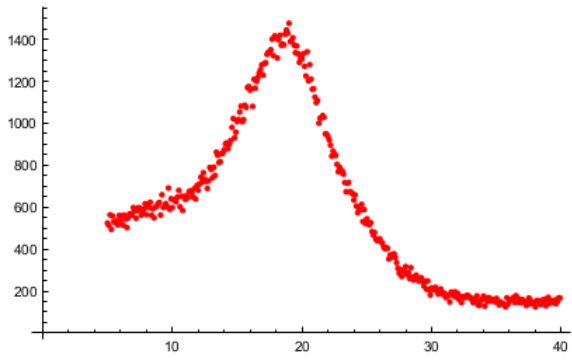
In[1]:= dataRead = Import["/home/haifa/Desktop/haifa/Data/655-1age1w.txt", "Table"];
dataRead[[1]]
Out[2]= {655-1age1w}

In[3]:= dR = Length[dataRead]
Out[3]= 10 502

In[4]:= dataIn = Table[dataRead[[i]], {i, 2, dR/3, 10}];
dataFull = Table[dataRead[[i]], {i, 2, dR}];
dF = Length[dataFull]

Out[6]= 10 501

In[7]:= dIn = Length[dataIn]
Out[7]= 350

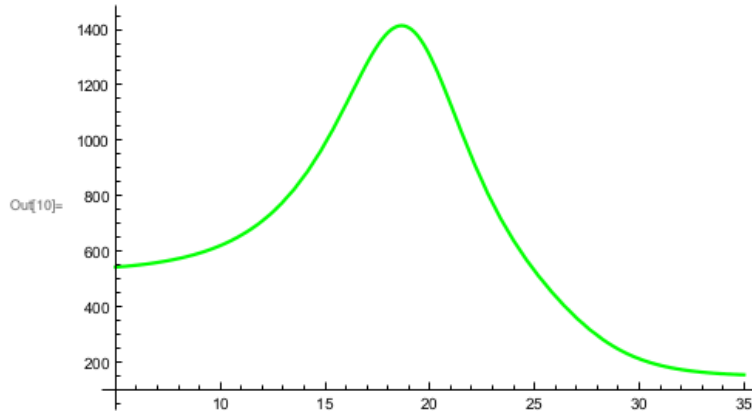
In[8]:= plotData =
ListPlot[dataIn, PlotRange → All, AxesOrigin → {0, 0}, PlotStyle → {Thick, Red}]
Out[8]=


In[9]:= y2 = FindFit[dataIn,  $\frac{A1}{e^{-a1(s-c1)} + e^{b1(s-c1)}} + \frac{A2}{(e^{-a2(s-c2)} + e^{b2(s-c2)})} + d$ , {{A1, 450}, {a1, 0.2}, {b1, 0.4}, {c1, 18}, {A2, 250}, {a2, 0.15}, {b2, 0.4}, {c2, 28}, {d, 30}}, s]
Out[9]= {A1 → 1819.42, a1 → 0.30624, b1 → 0.431262, c1 → 19.1545, A2 → 334.645, a2 → -0.00469194, b2 → 0.537871, c2 → 26.6047, d → 148.221}

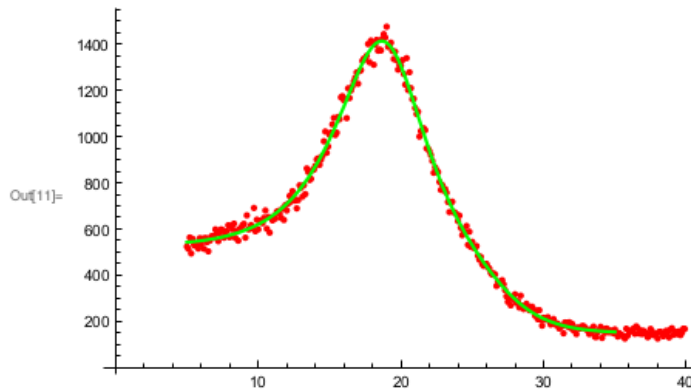
```



```
In[10]:= fitData = Plot[ReplaceAll[ $\frac{A1}{e^{-a1(s-c1)} + e^{b1(s-c1)}} + \frac{A2}{(e^{-a2(s-c2)} + e^{b2(s-c2)})} + d, y2],$ 
{s, 5, 35}, PlotRange -> All, PlotStyle -> {Thick, Green}]
```



```
In[11]:= Show[plotData, fitData]
```



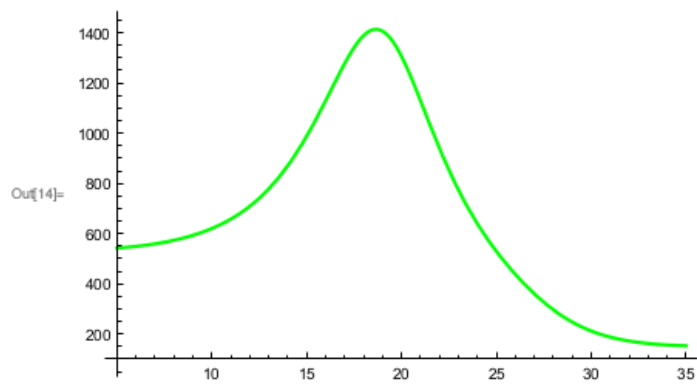
```
In[12]:=
```

```
y2 = FindFit[dataIn,  $\frac{A1}{e^{-a1(s-c1)} + e^{b1(s-c1)}} + \frac{A2}{(e^{-a2(s-c2)} + e^{b2(s-c2)})} + da + db s,$ 
{{A1, 450}, {a1, 0.2}, {b1, 0.4}, {c1, 18}, {A2, 250},
{a2, 0.15}, {b2, 0.4}, {c2, 28}, {da, 30}, {db, -1}}, s]
```

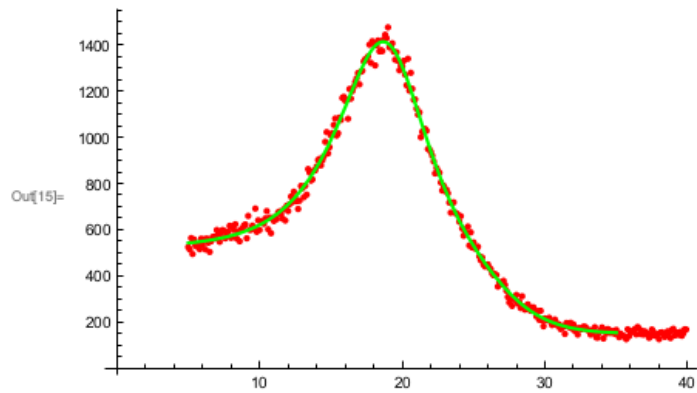
```
Out[12]:= {A1 -> 1809.32, a1 -> 0.309718, b1 -> 0.428425, c1 -> 19.128, A2 -> 357.179,
a2 -> -0.00507351, b2 -> 0.506348, c2 -> 26.5497, da -> 116.522, db -> 0.843387}
```

```
In[14]:= fitData = Plot[ReplaceAll[ $\frac{A1}{e^{-a1(s-c1)} + e^{b1(s-c1)}} + \frac{A2}{(e^{-a2(s-c2)} + e^{b2(s-c2)})} + da + db s, y2],$   

{s, 5, 35}, PlotRange -> All, PlotStyle -> {Thick, Green}]
```



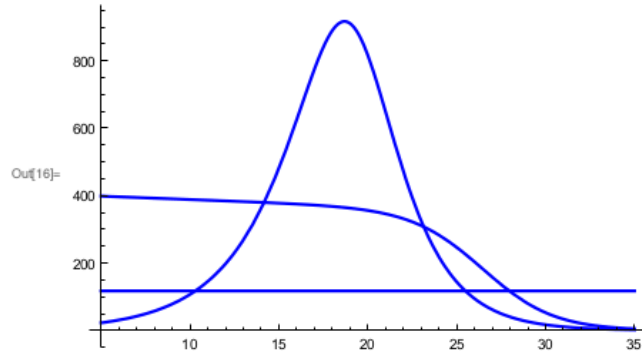
```
In[15]:= Show[plotData, fitData]
```



```

In[16]:= fitParts = Plot[ {ReplaceAll[ $\frac{A1}{e^{-a1 (s-c1)} + e^{b1 (s-c1)}}$ , y2],
    ReplaceAll[ $\frac{A2}{(e^{-a2 (s-c2)} + e^{b2 (s-c2)})}$ , y2], ReplaceAll[da + db, y2]}, {s, 5, 35},
    PlotRange -> All, PlotStyle -> {{Thick, Blue}, {Thick, Blue}, {Thick, Blue}}]

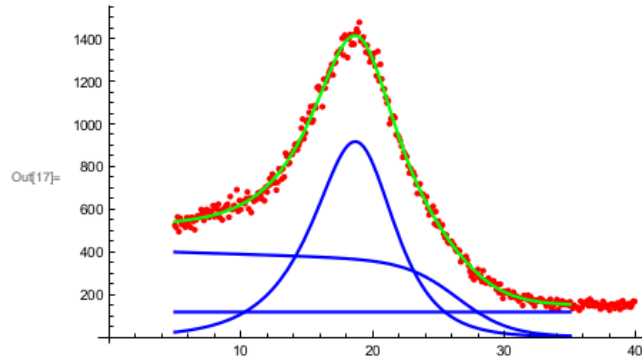
```



```

In[17]:= Show[plotData, fitData, fitParts]

```



```

In[18]:=

```

```

wts = Table[dataIn[[i]], {i, 1, dIn}];
nlm = NonlinearModelFit[dataFull,  $\frac{A1}{e^{-a1 (s-c1)} + e^{b1 (s-c1)}} + \frac{A2}{(e^{-a2 (s-c2)} + e^{b2 (s-c2)})} + da + db s,$ 
    {{A1, 450}, {a1, 0.2}, {b1, 0.4}, {c1, 18}, {A2, 100},
    {a2, 0.15}, {b2, 0.4}, {c2, 28}, {da, 30}, {db, -1}}, s]

```

```

Out[18]= FittedModel[ $188.109 + \frac{322.373}{e^{0.00193709 (-26.4545 + s)} + e^{0.558893 (\ll 1 \gg)}} + \frac{1816.4}{e^{-0.309592 (\ll 1 \gg)} + e^{\ll 18 \gg (-\ll 19 \gg + s)}} - 1.22373 s$ ]

```

In[19]:= **Normal[nlm]**

$$\text{Out[19]} = 188.109 + \frac{322.373}{e^{0.00193709 (-26.4545+s)} + e^{0.558893 (-26.4545+s)}} + \frac{1816.4}{e^{-0.309592 (-19.0361+s)} + e^{0.410388 (-19.0361+s)}} - 1.22373 s$$

In[20]:= **y2 = nlm["BestFitParameters"]**

Out[20]= {A1 → 1816.4, a1 → 0.309592, b1 → 0.410388, c1 → 19.0361, A2 → 322.373, a2 → -0.00193709, b2 → 0.558893, c2 → 26.4545, da → 188.109, db → -1.22373}

In[21]:= **nlm["EstimatedVarirance"]**

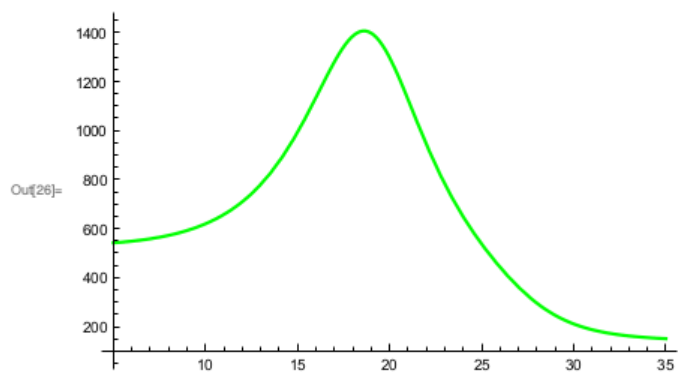
$$\text{Out[21]} = 188.109 - 1.22373 \text{ EstimatedVarirance} + \frac{322.373}{\left(e^{0.00193709 (-26.4545+\text{EstimatedVarirance})} + e^{0.558893 (-26.4545+\text{EstimatedVarirance})} \right)} + \frac{1816.4}{\left(e^{-0.309592 (-19.0361+\text{EstimatedVarirance})} + e^{0.410388 (-19.0361+\text{EstimatedVarirance})} \right)}$$

In[23]:= **nlm["ParameterConfidenceIntervalTable", ConfidenceLevel → 0.99]**

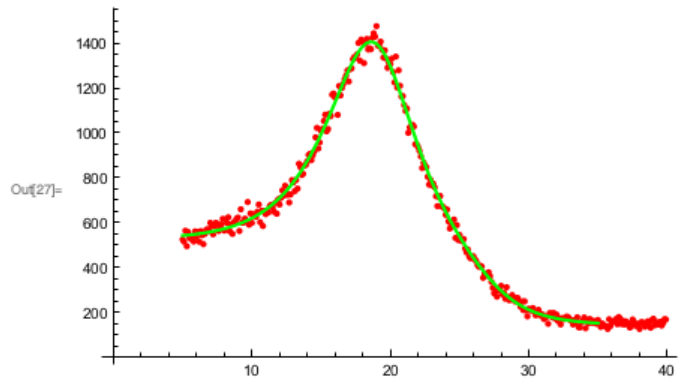
	Estimate	Standard Error	Confidence Interval
A1	1816.4	16.4185	{1774.1, 1858.7}
a1	0.309592	0.00317409	{0.301415, 0.31777}
b1	0.410388	0.0040637	{0.399918, 0.420857}
c1	19.0361	0.0257756	{18.9696, 19.1025}
A2	322.373	14.8753	{284.049, 360.696}
a2	-0.00193709	0.00213406	{-0.00743507, 0.00356089}
b2	0.558893	0.0142962	{0.522061, 0.595724}
c2	26.4545	0.124132	{26.1347, 26.7743}
da	188.109	0.709662	{186.281, 189.937}
db	-1.22373	0.00939877	{-1.24795, -1.19952}

```
In[26]:= fitData = Plot[ReplaceAll[ $\frac{A1}{e^{-a1(s-c1)} + e^{b1(s-c1)}} + \frac{A2}{(e^{-a2(s-c2)} + e^{b2(s-c2)})} + da + db s, y2],$   

{s, 5, 35}, PlotRange -> All, PlotStyle -> {Thick, Green}]
```



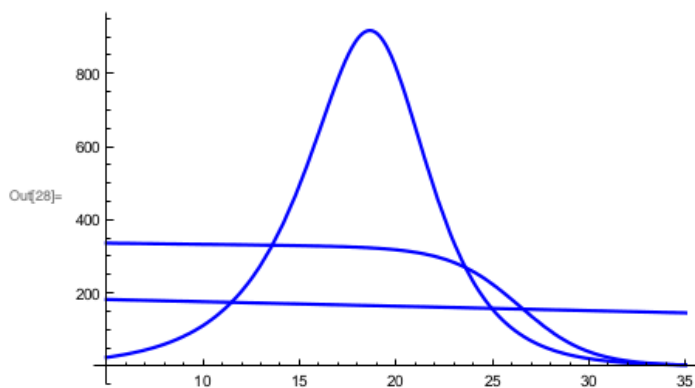
```
In[27]:= Show[plotData, fitData]
```



```

In[28]:= fitParts = Plot[{ReplaceAll[ $\frac{A1}{e^{-a1(s-c1)} + e^{b1(s-c1)}}$ , y2],
  ReplaceAll[ $\frac{A2}{(e^{-a2(s-c2)} + e^{b2(s-c2)})}$ , y2], ReplaceAll[da + db s, y2]}, {s, 5, 35},
  PlotRange -> All, PlotStyle -> {{Thick, Blue}, {Thick, Blue}, {Thick, Blue}}]

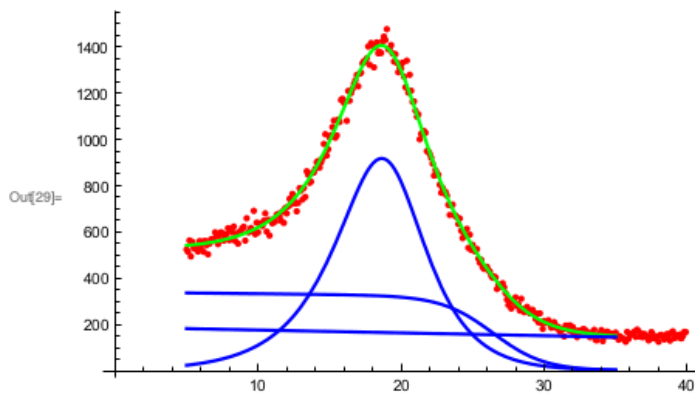
```



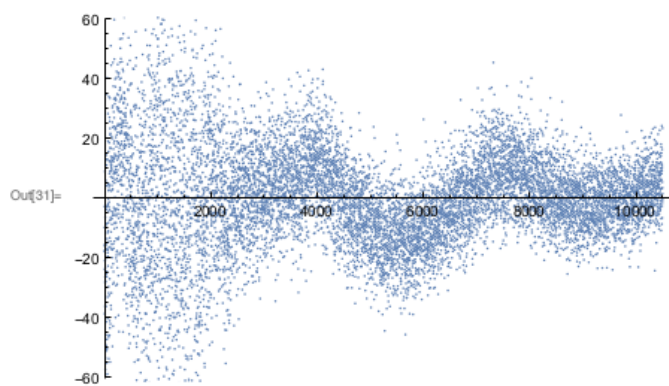
```

In[29]:= Show[plotData, fitData, fitParts]

```

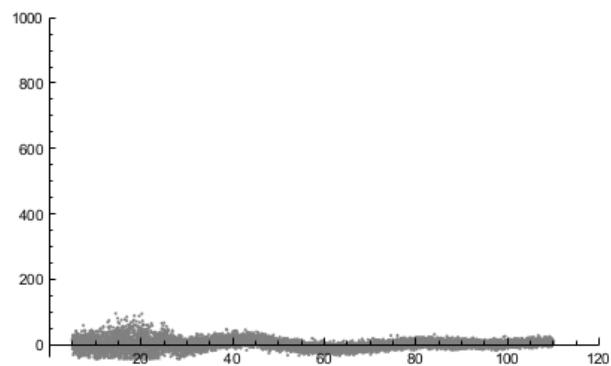


```
In[30]:= resi = nlm["FitResiduals"];
ListPlot[resi]
```

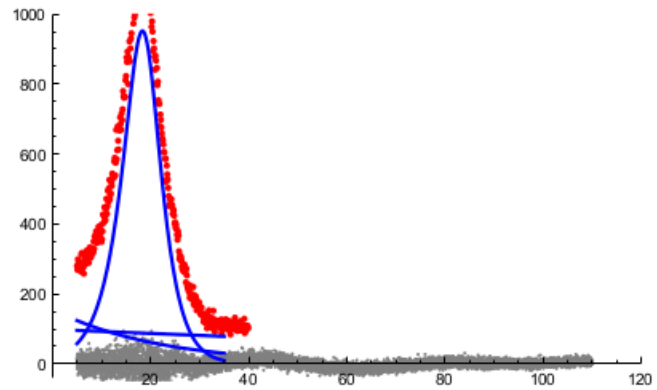


```
resiData = Table[{dataFull[[i, 1]], resi[[i]]}, {i, 1, dF}];
```

```
resiplot =
ListPlot[resiData, PlotRange -> {{0, 120}, {-40, 1000}}, PlotStyle -> {Thick, Gray}]
```



```
Show[resiplot, plotData, fitParts]
```



```
In[32]:=
```

```
y7 = FindFit[dataIn,  $\frac{A1}{(e^{-a1(s-c1)} + e^{b1(s-c1)})} + \frac{A1}{(e^{-a1(s+c1)} + e^{b1(s+c1)})} +$   

 $\frac{A2}{(e^{-a2(s-c2)} + e^{b2(s-c2)})} + \frac{A2}{(e^{-a2(s+c2)} + e^{b2(s+c2)})} + d$ , {{A1, 450}, {a1, 0.2},  

{b1, 0.4}, {c1, 18}, {A2, 250}, {a2, 0.15}, {b2, 0.4}, {c2, 28}, {d, 30}}, s]
```

```
Out[32]= {A1 → 1819.23, a1 → 0.306229, b1 → 0.431341, c1 → 19.1548,  

A2 → 334.803, a2 → -0.00466435, b2 → 0.53782, c2 → 26.6039, d → 148.222}
```



```
y2[s] = {A1 → 277.5710978720899`, a1 → 0.3638434180114862`, b1 → 0.4928733076208165`,
c1 → 18.421578993973988`, A2 → 231.4188420545929`, a2 → 0.06964405932635563`,
b2 → 0.4061139086592587`, c2 → 23.05270607189448`, d → 24.96340490857636`}
```

Set::write : Tag List in

```
{A1 → 286.444, a1 → 0.320524, b1 → 0.476202, c1 → 18.8637, A2 → 220.041, a2 → 0.071692, b2 → 0.335259,
c2 → 22.3499, da → 28.5434, db → -0.15563}[s] is Protected. >>
```

```
Out[52]= {A1 → 277.571, a1 → 0.363843, b1 → 0.492873, c1 → 18.4216,
A2 → 231.419, a2 → 0.0696441, b2 → 0.406114, c2 → 23.0527, d → 24.9634}
```

```
In[53]:=
```

```
x2r[s] = (277.5710978720899 /
(e^(-0.3638434180114862 (s-18.421578993973988)) + e^0.4928733076208165 (s-18.421578993973988))) +
231.4188420545929 / (e^(-0.06964405932635563 (s-23.05270607189448)) +
e^0.4061139086592587 (s-23.05270607189448))) + 24.96340490857636
Out[53]= 24.9634 +  $\frac{231.419}{e^{-0.0696441 (-23.0527+s)} + e^{0.406114 (-23.0527+s)}}$  +  $\frac{277.571}{e^{-0.363843 (-18.4216+s)} + e^{0.492873 (-18.4216+s)}}$ 
```

y7[s] =

```
In[54]:= {A1 → 509.26804382945704`, a1 → 0.18021665481838156`,
b1 → 0.35176770634788335`, c1 → 19.704103138932012`, A2 → 35.18416392883497`,
a2 → -0.01064054098698481`, b2 → 0.010640541070043339`,
c2 → 22.805628548908352`, q1 → 2803.0911912388146`, q2 → 2.2493297879762038`}
```

```
Out[54]= {A1 → 509.268, a1 → 0.180217, b1 → 0.351768, c1 → 19.7041, A2 → 35.1842,
a2 → -0.0106405, b2 → 0.0106405, c2 → 22.8056, q1 → 2803.09, q2 → 2.24933}
```

$$\text{Sum}\left[\frac{1}{10\,502}\left(24.96340490857636^{\cdot} + \frac{231.4188420545929^{\cdot}}{e^{-0.06964405932635563^{\cdot}}(-23.05270607189448^{\cdot}+s) + e^{0.4061139086592587^{\cdot}}(-23.05270607189448^{\cdot}+s)} + \frac{277.5710978720899^{\cdot}}{e^{-0.3638434180114862^{\cdot}}(-18.421578993973988^{\cdot}+s) + e^{0.4928733076208165^{\cdot}}(-18.421578993973988^{\cdot}+s)} + \frac{35.18416392883497^{\cdot}}{e^{-0.01064054098698481^{\cdot}}(-22.805628548908352^{\cdot}+s) + e^{0.010640541070043339^{\cdot}}(-22.805628548908352^{\cdot}+s)} + \frac{509.26804382945704^{\cdot}}{e^{-0.18021665481838156^{\cdot}}(-19.704103138932012^{\cdot}+s) + e^{0.35176770634788335^{\cdot}}(-19.704103138932012^{\cdot}+s)} + \frac{509.26804382945704^{\cdot}}{e^{-0.18021665481838156^{\cdot}}(19.704103138932012^{\cdot}+s) + e^{0.35176770634788335^{\cdot}}(19.704103138932012^{\cdot}+s)} + \frac{35.18416392883497^{\cdot}}{e^{-0.01064054098698481^{\cdot}}(22.805628548908352^{\cdot}+s) + e^{0.010640541070043339^{\cdot}}(22.805628548908352^{\cdot}+s)} + \frac{862.6674958052437^{\cdot}}{s^2}\right), \{s, 5, 35\} \right]$$

$$\text{Out}[56]= 24.9634 + \frac{231.419}{e^{-0.0696441}(-23.0527+s) + e^{0.406114}(-23.0527+s)} + \frac{277.571}{e^{-0.363843}(-18.4216+s) + e^{0.492873}(-18.4216+s)}$$

$$\text{Out}[57]= 0.837533$$

XRD samples	Specimen ID
T1	655-1age1W
T2	655-2age1W
T3	655-3age1W
T4	655-4age1W
T5	655-5age1W
T6	655-6age1W
T7	655-7age1W
L1	RR1Lage1W
L2	RR2Lage1W
L3	RR3Lage1W
L4	RR4Lage1W
L5	RR5Lage1W
L6	RR6Lage1W
L7	RR7Lage1W
H1	HearstAage1W
H2	HearstBage1W
N1	HWY11-5102age1W
N2	HWY11-5108age1W
N3	HWY11-5106age1W
E9	E009age1W
AAE	AAEageW
O1	SC58-34
O2	PC58-34

Bibliography

- [1] (www.eapa.org/asphalt)
- [2] (www.travel.ru/wow/pitch_lake.html)
- [3] (wsmtl.engr.wisc.edu)
- [4] (www.pavementinteractive.org/article/rutting)
- [5] Yen, T. F., and Chilingarian, G. V. (Eds.). (2000). *Asphaltenes and Asphalts*, 2 (Vol.40). Elsevier
- [6] Speight, J. G. (1999). The Chemical and Physical Structure of Petroleum: Effects on Recovery Operations. *Journal of Petroleum Science and Engineering*, 22(1), 3-15.
- [7] Hesp, S.A.M., (2008). Low-Temperature Fracture in Asphalt Binders, Mastics, and Mixtures In; *Modeling of Asphalt Concrete*, Y. Richard (Ed.), American Society for Civil Engineering, (15), 429-453.
- [8] Galal, K., and White, T. (2001). Correlations between Superpave Asphalt Stiffnesses and In-Service Pavement Performance. *Transportation Research Record: Journal of the Transportation Research Board*, (1766), 57-66.
- [9] Dickie, J. P., and Yen, T. F. (1967). Macrostructures of the Asphaltic Fractions by Various Instrumental Methods. *Analytical Chemistry*, 39(14), 1847-1852.

- [10] Yen, T. F. (1974). Structure of Petroleum Asphaltene and its Significance. Energy Sources, Part a Recovery, Utilization, and Environmental Effects, 1(4), 447-463.
- [11] Yen, T. F., Erdman, J. G., and Pollack, S. S. (1961). Investigation of the Structure of Petroleum Asphaltenes by X-ray Diffraction. Analytical Chemistry, 33(11), 1587-1594.
- [12] Christopher, J., Sarpal, A. S., Kapur, G. S., Krishna, A., Tyagi, B. R., Jain, M. C., and Bhatnagar, A. K. (1996). Chemical Structure of Bitumen-Derived Asphaltenes by Nuclear Magnetic Resonance Spectroscopy and X-Ray Diffractometry. Fuel, 75(8), 999-1008.
- [13] Shirokoff, J. W., Siddiqui, M. N., and Ali, M. F. (1997). Characterization of the Structure of Saudi Crude Asphaltenes by X-ray Diffraction. Energy and Fuels, 11(3), 561-565.
- [14] Sedeghi, M.A., Chilingarian, G.V. and Yen, T.F. (1986). American Chemical Society Symp. Ser. G.99 (Chem. Abstr. 104: 151905R).
- [15] Michael, G., Al-Siri, M., Khan, Z. H., and Ali, F. A. (2005). Differences in Average Chemical Structures of Asphaltene Fractions Separated From Feed and Product Oils of a Mild Thermal Processing Reaction. Energy and Fuels, 19(4), 1598-1605.
- [16] Siddiqui, M. N., Ali, M. F., and Shirokoff, J. (2002). Use of X-ray Diffraction in Assessing the Aging Pattern of Asphalt Fractions. Fuel, 81(1), 51-58.
- [17] Schwager, I., Farmanian, P. A., Kwan, J. T., Weinberg, V. A., and Yen, T. F. (1983). Characterization of the Microstructure and Macrostructure of Coal-

- Derived Asphaltenes by Nuclear Magnetic Resonance Spectrometry and X-Ray Diffraction. *Analytical Chemistry*, 55(1), 42-45.
- [18] Decroocq, D., Thomas, M., Fixari, B., Leperchec, P., Bigois, M., Lena, L., and Rossarie, J. (1992). Improving Heat-Treatment Processes for Residues by Optimizing the Transformation of Resins and Asphaltenes. *Revue De L'institut Francais du Petrole*, 47(1), 103.
- [19] Ebert, L. B., Mills, D. R., and Scanlon, J. C. (1983). X-ray Diffraction Of N-Paraffins and Stacked Aromatic Molecules: Problems in Using Diffraction to Determine the Average Structure of Asphaltenes. *Am. Chem. Soc., Div. Pet. Chem., Prepr.;*(United States), 28(CONF-830814-).
- [20] Mullins, O. C. (2010). The Modified Yen Model. *Energy and Fuels*, 24(4), 2179-2207.
- [21] Aldea, N., Tiusan, C. V., and Barz, B. (2004). A New X-ray Line Profile Approximation Used for the Evaluation of the Global Nanostructure of Nickel Clusters. *Journal of Optoelectronics and Advanced Materials*, 6(1), 225-235
- [22] Gebresellasie, K., Shirokoff, J., and Lewis, J. C. (2012). Effect of X-ray Line Spectra Profile Fitting with Pearson VII, Pseudo-Voigt and Generalized Fermi Functions on Asphalt Binder Aromaticity and Crystallite Parameters. In *Journal of Physics: Conference Series* (Vol. 397, No. 1, p. 012069). IOP Publishing.
- [23] Gebresellasie, K., Lewis, J. C., and Shirokoff, J. (2013). X-ray Spectral Line Shape Analysis of Asphalt Binders. *Energy and Fuels*, 27(4), 2018-2024.
- [24] Deacon, J. A., Tsai, B. W., and Monismith, C. L. (1995). Fatigue Performance of Asphalt Concrete Mixes and its Relationship to Asphalt Concrete Pavement

- Performance in California (No. RTA-65W485-2). University of California Berkeley, Institute of Transportation Studies, Asphalt Research Program.
- [25] Yasar, M., Akmaz, S., and Gurkaynak, M. A. (2009). Investigation of the Molecular Structure of Turkish Asphaltenes. *Petroleum Science and Technology*, 27(10), 1044-1061.
 - [26] Trejo, F., Ancheyta, J., Morgan, T. J., Herod, A. A., and Kandiyoti, R. (2007). Characterization of Asphaltenes from Hydrotreated Products by SEC, LDMS, MALDI, NMR, and XRD. *Energy and Fuels*, 21(4), 2121-2128.
 - [27] Andersen, S. I., Jensen, J. O., and Speight, J. G. (2005). X-ray Diffraction of Subfractions of Petroleum Asphaltenes. *Energy and Fuels*, 19(6), 2371-2377.
 - [28] Hesp, S. A., Iliuta, S., and Shirokoff, J. W. (2007). Reversible Aging in Asphalt Binders. *Energy and Fuels*, 21(2), 1112-1121.
 - [29] Yang, S. F., Chiu, W. T., Wang, T. M., Lee, W. C., Chen, C. L., Tzeng, C. C. (2009). Asphalt Concrete and Permeable Brick Produced from Incineration Ash using Thermal Plasma Technology. *Journal of Environmental Engineering and Management*, 19(4), 221-226.
 - [30] Mazaheri Assadi, M., Tabatabaee, M. S. (2010). Biosurfactants and Their Use in Upgrading Petroleum Vacuum Distillation Residue: A Review. *International Journal of Environmental Research*, 4(4), 549-572.
 - [31] Mullins, O. C., Sabbah, H., Eyssautier, J., Pomerantz, A. E., Barre', L., Andrews, A. B., Lepkowicz, R. (2012). Advances in Asphaltene Science and the Yen-Mullins model. *Energy and Fuels*, 26(7), 3986-4003.

- [32] McCarron, B., Yu, X., Tao, M., Burnham, N. (2011-2012). The Investigation of “Bee-Structures” in Asphalt Binders. Major Qualifying Project. Department of Physics, Worcester Polytechnical Institute.
- [33] AlHumaidan, F. S., Hauser, A., Rana, M. S., Lababidi, H. M., Behbehani, M. (2015). Changes in Asphaltene Structure During Thermal Cracking of Residual Oils: XRD Study. *Fuel*, 150, 558-564.
- [34] Pecharsky, V. K., and Zavalij, P. Y. (2009). *Fundamentals of Powder Diffraction and Structural Characterization of Materials* (Vol. 69). New York: Springer.
- [35] H. Alqahtani, J. C. Lewis, J, Shirokoff, Modeling X-ray Line Shapes from Asphaltenes, 23th International Conference on Spectral Line Shapes (ICSLS), American Institute of Physics, J. Phys: Conf. Torun, Poland, (2016), pp.1-5.
- [36] H. Alqahtani, J. C. Lewis, J, Shirokoff, Effect of Computer Modeling X-ray Spectral Line Shapes of Asphaltenes Using Different Background, Proceedings of the Newfoundland Electrical and Computer Engineering Conference (NECEC). St. John's, NL, (IEEE) Newfoundland and Labrador Section, Nov. 5, (2015), pp.1-4.
- [37] H. Alqahtani, J. C. Lewis, J, Shirokoff, Modeling X-ray Line Shapes of Asphaltenes, Proceeding of the Women in Physics Canada Conference (WIPC), Toronto, ON, July 30-Aug 1. 2015
- [38] Andersen, S. I., Jensen, J. O., Speight, J. G. (2005). X-ray Diffraction of Subfractions of Petroleum Asphaltenes. *Energy and Fuels*, 19(6), 2371-2377.
- [39] Lee, K. W., and Mahboub, K. C. (2006). *Asphalt Mix Design and Construction: Past, Present, and Future*. American Society of Civil Engineers.

- [40] Speight, T. F., Yen, J. G., Chilingarian, G. V. (1994). Asphaltenes and Asphalts, 1. Developments in Petroleum Science, 40 A.
- [41] Zakar, P. (1971). Asphalt. Chemical Publishing Company , INC. New York.
- [42] Akbarzadeh, K., Hammami, A., Kharrat, A., Zhang, D., Allenson, S., Creek, J. Mullins, O. C. (2007). Asphaltenes Problematic but Rich in Potential. Oilfield Review, 19(2), 22-43.
- [43] Delhez, R., De Keijser, T. H., Mittemeijer, E. J. (1982). Determination of Crystallite Size and Lattice Distortions Through X-ray Diffraction Line Profile Analysis. Fresenius' Zeitschrift for Analytische Chemie, 312(1), 1-16.
- [44] Rahimi, P. M., Gentzis, T. (2006). The Chemistry of Bitumen and Heavy Oil Processing. In Practical Advances in Petroleum Processing (pp. 597-634). Springer New York. Chapter 19, Vol. 2, pp (149-186).
- [45] Airey, G. D. (2003). Rheological Properties of Styrene Butadiene Styrene Polymer Modified Road Bitumens. Fuel, 82(14), 1709-1719.
- [46] Aldea, N., Tiusan, C. V., Barz, B. (2004). A New X-ray Line Profile Approximation Used for the Evaluation of the Global Nanostructure of Nickel Clusters. J. Opt. Adv. Mat, 6(1), 225.
- [47] Ali, L. H. (1971). A Method for the Calculation of Molecular Weights of Aromatic Compounds, and its Application to Petroleum Fractions. Fuel, 50(3), 298-307.
- [48] Christy, A. A., Dahl, B., Kvalheim, O. M. (1989). Structural Features of Resins, Asphaltenes and Kerogen Studied by Diffuse Reflectance Infrared Spectroscopy. Fuel, 68(4), 430-435.

- [49] Gawel, I., Baginska, K. (2004). Effect of Chemical Nature on the Susceptibility of Asphalt to Aging. *Petroleum Science and Technology*, 22(9-10), 1261-1271.
- [50] Ergun, S., Tiensuu, V. H. (1959). Interpretation of the Intensities of X-rays Scattered by Coals. *Fuel*, 38(1), 64-78.
- [51] Goual, L., Sedghi, M., Zeng, H., Mostowfi, F., McFarlane, R., Mullins, O. C. (2011). On the Formation and Properties of Asphaltene Nanoaggregates and Clusters by DC-conductivity and Centrifugation. *Fuel*, 90(7), 2480-2490.
- [52] Groenzin, H., Mullins, O. C. (1999). Asphaltene Molecular Size and Structure. *The Journal of Physical Chemistry A*, 103(50), 11237-11245.
- [53] Groenzin, H., Mullins, O. C. (2000). Molecular Size and Structure of Asphaltenes from Various Sources. *Energy and Fuels*, 14(3), 677-684.
- [54] Harrison, I. R., Wang, G., Hsu, T. C. (1992). A Differential Scanning Calorimetry Study of Asphalt Binders (No. SHRP-A/UFR-92-612).
- [55] Howard, S. A., Preston, K. D. (1989). Profile Fitting of Powder Diffraction Patterns. Pp. 217-275 in: *Modern Powder Diffraction* (DL Bish and JE Post, editors). *Reviews in Mineralogy*, 20.
- [56] Gawrys, K. L., Matthew Spiecker, P., Kilpatrick, P. K. (2003). The Role of Asphaltene Solubility and Chemical Composition on Asphaltene Aggregation. *Petroleum Science and Technology*, 21(3-4), 461-489.
- [57] Kim, Y. R. (2008). *Modeling of Asphalt Concrete*, MH/ASCE, First Edition.
- [58] Koots, J. A., Speight, J. G. (1975). Relation of petroleum resins to asphaltenes. *Fuel*, 54(3), 179-184.

- [59] Langford, J. I., Wilson, A. J. C. (1978). Scherrer After Sixty Years: A Survey and Some New Results in the Determination of Crystallite Size. *Journal of Applied Crystallography*, 11(2), 102-113.
- [60] Lee, S. J., Amirkhanian, S. N., Park, N. W., Kim, K. W. (2009). Characterization of Warm Mix Asphalt Binders Containing Artificially Long-Term Aged Binders. *Construction and Building Materials*, 23(6), 2371-2379.
- [61] Lu, X., Soenen, H., Redelius, P. (2004, May). Impact of Bitumen Wax on Asphalt Performance-Low Temperature Cracking. In *Proceeding of the Third Eurobitumen and Euraspalt Congress*.
- [62] Mullins, O. C. (2011). The Asphaltenes. *Annual Review of Analytical Chemistry*, 4, 393-418.
- [63] Mullins, O. C., Sheu, E. Y., Hammami, A., Marshall, A. G. (2007). *Asphaltenes, Heavy Oils, and Petroleomics*. Springer Science and Business Media.
- [64] Joshi, N. B., Mullins, O. C., Jamaluddin, A., Creek, J., McFadden, J. (2001). Asphaltene Precipitation from Live Crude Oil. *Energy and Fuels*, 15(4), 979-986.
- [65] Ravey, J. C., Ducouret, G., Espinat, D. (1988). Asphaltene Macrostructure by Small Angle Neutron Scattering. *Fuel*, 67(11), 1560-1567.
- [66] Fortier, R., Vinson, T. (1998). Low-Temperature Cracking and Aging Performance of Modified Asphalt Concrete Specimens. *Transportation Research Record: Journal of the Transportation Research Board*, (1630), 77-86.
- [67] Roberts, F. L., Kandhal, P. S., Brown, E. R., Lee, D. Y. Kennedy, T. W. (1991). *Hot Mix Asphalt Materials, Mixture Design and Construction*.
- [68] <http://construction.about.com/od/Earthwork/a/Hot-Mix-Asphalt-Types.htm>

- [69] <http://www.state.nj.us/transportation/eng/pavement/pdf/HotMix0709.pdf>
- [70] Roque, R., Birgisson, B., Sangpetngam, B., Zhang, Z. (2002). Hot Mix Asphalt Fracture Mechanics: A Fundamental Crack Growth Law for Asphalt Mixtures. *Journal of the Association of Asphalt Paving Technologists*, 71.
- [71] Kristjánssdóttir, Ó., Muench, S., Michael, L., Burke, G. (2007). Assessing Potential for Warm-Mix Asphalt Technology Adoption. *Transportation Research Record: Journal of the Transportation Research Board*, (2040), 91-99.
- [72] Raynaud, G. M., Lafon, J. F., Brosseaud, Y., Beghin, A. (2007). Cold Mix Asphalt. In *Choice for Sustainable Development. Pre-Proceedings of the 23rd PI-ARRC World Road Congress*.
- [73] Sheu, E. Y. (2002). Petroleum Asphaltene Properties, Characterization, and Issues. *Energy and Fuels*, 16(1), 74-82.
- [74] Stastna, J., Zanzotto, L., Vacin, O. J. (2003). Viscosity Function in Polymer-Modified Asphalts. *Journal of Colloid and Interface Science*, 259(1), 200-207.
- [75] Strausz, O. P., Mojelsky, T. W., Lown, E. M. (1992). The Molecular Structure of Asphaltene. An Unfolding Story. *Fuel*, 71(12), 1355-1363.
- [76] Wu, S., Cong, P., Yu, J., Luo, X., Mo, L. (2006). Experimental Investigation of Related Properties of Asphalt Binders Containing Various Flame Retardants. *Fuel*, 85(9), 1298-1304.
- [77] Yapp, M. T., Durrani, A. Z., Finn, F. N. (1991). HP-GPC and Asphalt Characterization Literature Review (No. SHRP-A/UIR-91-503).

- [78] Yu, J. Y., Feng, P. C., Zhang, H. L., Wu, S. P. (2009). Effect of Organo-Montmorillonite on Aging Properties of Asphalt. *Construction and Building Materials*, 23(7), 2636-2640.
- [79] Bayat, M., Sattarin, M., Teymouri, A. (2008). Prediction of Asphaltene Self-Precipitation in Dead Crude Oil. *Energy and Fuels*, 22(1), 583-586.
- [80] Christopher, J., Sarpal, A. S., Kapur, G. S., Krishna, A., Tyagi, B. R., Jain, M. C. Bhatnagar, A. K. (1996). Chemical Structure of Bitumen-Derived Asphaltenes by Nuclear Magnetic Resonance Spectroscopy and X-ray Diffractometry. *Fuel*, 75(8), 999-1008.